

1 **The evolution of biomass-burning aerosol size distributions due to**
2 **coagulation: dependence on fire and meteorological details and**
3 **parameterization**

4

5 **K.M. Sakamoto¹, J.R. Laing², R.G. Stevens³, D.A. Jaffe^{2,4}, and J. R. Pierce^{1,5}**

6

7 [1] Colorado State University, Fort Collins, CO, USA

8 [2] University of Washington-Bothell, Bothell, WA, USA

9 [3] University of Leeds, Leeds, UK

10 [4] University of Washington, Seattle, WA, USA

11 [5] Dalhousie University, Halifax, NS, Canada

12

13 Corresponding author: J.R. Pierce (jeffrey.pierce@colostate.edu)

14

15 **Abstract**

16 Biomass-burning aerosols have a significant effect on global and regional aerosol climate forcings. To
17 model the magnitude of these effects accurately requires knowledge of the size distribution of the
18 emitted and evolving aerosol particles. Current biomass-burning inventories do not include size
19 distributions, and global and regional models generally assume a fixed size distribution from all
20 biomass-burning emissions. However, biomass-burning size distributions evolve in the plume due to
21 coagulation and net organic aerosol (OA) evaporation or formation, and the plume processes occur on
22 spacial scales smaller than global/regional-model grid boxes. The extent of this size-distribution
23 evolution is dependent on a variety of factors relating to the emission source and atmospheric
24 conditions. Therefore, to account for biomass-burning aerosol size in global models accurately requires
25 an *effective* aerosol size distribution that accounts for this sub-grid evolution and can be derived from
26 available emissions-inventory and meteorological parameters.

27 In this paper, we perform a detailed investigation of the effects of coagulation on the aerosol size
28 distribution in biomass-burning plumes. We compare the effect of coagulation to that of OA
29 evaporation and formation. We develop coagulation-only parameterizations for effective biomass-

30 burning size distributions using the SAM-TOMAS large-eddy simulation plume model. For the most-
31 sophisticated parameterization, we use the Gaussian Emulation Machine for Sensitivity Analysis
32 (GEM-SA) to build a parameterization of the aged size distribution based on the SAM-TOMAS output
33 and seven inputs: emission median dry diameter, emission distribution modal width, mass emissions
34 flux, fire area, mean boundary-layer wind speed, plume mixing depth, and time/distance since
35 emission. This parameterization was tested against an independent set of SAM-TOMAS simulations,
36 and yields R^2 values of 0.83 and 0.89 for D_{pm} and modal width, respectively. The size distribution is
37 particularly sensitive to the mass emissions flux, fire area, wind speed, and time, and we provide
38 simplified fits of the aged size distribution to just these input variables. The simplified fits were tested
39 against eleven aged biomass-burning size distributions observed at the Mt. Bachelor Observatory in
40 August 2015. The simple fits captured over half of the variability in observed D_{pm} and modal width
41 even though the freshly emitted D_{pm} and modal widths were unknown. These fits may be used in global
42 and regional aerosol models. Finally, we show that coagulation generally leads to greater changes in the
43 particle size distribution than does OA evaporation/formation using estimates of OA production/loss
44 from the literature.

45 **1. Introduction**

46 ***1.1 Biomass-burning aerosols***

47 Biomass burning (including wildfires, prescribed fires, and agricultural fires) releases significant
48 amounts of gas- and particle-phase species to the atmosphere (Andreae and Merlet, 2001; Reid et al.,
49 2005). The particle-phase emissions are composed primarily of a mixture of organic aerosol (OA) and
50 black carbon (BC) with some inorganic species (e.g. potassium), and the ratios of these species depend
51 on the source fire conditions (Capes et al., 2008; Carrico et al., 2010; Cubison et al., 2011; Hecobian et
52 al., 2011; Hennigan et al., 2011; Reid et al., 2005). These aerosols affect the global radiation budget
53 through the indirect and direct aerosol effects (Boucher et al., 2013). The smoke particles themselves
54 are able to act as cloud condensation nuclei (CCN) and increase cloud albedo and lifetime (indirect
55 aerosol effect; Lee et al., 2013; Pierce et al., 2007; Spracklen et al., 2011) as well as
56 scattering/absorbing incoming solar-radiation directly (direct aerosol effect; Alonso-Blanco et al., 2014;
57 Boucher et al., 2013; Haywood and Boucher, 2000; Jacobson, 2001).

58 Particle size has a significant effect on the magnitude of both the direct and indirect aerosol

59 effects (Lee et al., 2013; Seinfeld and Pandis, 2006; Spracklen et al., 2011). The composition and
60 diameter of the particles affect their absorption/scattering efficiencies, which dictate the amount of
61 solar radiation absorbed/scattered per emitted mass of particles (Seinfeld and Pandis, 2006). Particle
62 diameter and hygroscopicity determine the particles' ability to act as a CCN and influence cloud
63 processes, and the total number of emitted particles increases with decreased particle size if total mass
64 emissions are fixed. Spracklen et al., (2011) found that a reduction by a factor of two in particle size for
65 all carbonaceous aerosols (for a fixed total aerosol mass) resulted in a ~300% increase in the cloud
66 albedo indirect effect globally, as more particles were available to act as CCN. Lee et al., (2013)
67 determined that CCN concentrations in the GLOMAP model were very sensitive to uncertainties in
68 biomass-burning emission diameter on both the regional and global scale (its attributable CCN
69 uncertainty ranked third of 28 factors tested globally). Therefore, to ascertain the role of biomass-
70 burning aerosols in climate forcings accurately, biomass-burning size distributions must be well
71 represented in aerosol-climate models.

72 Size distributions are subject to physical and chemical processing in the plume. The formation of
73 secondary organic aerosol (SOA) has been observed in lab studies of biomass-burning aerosol
74 (Cubison et al., 2011; Grieshop et al., 2009; Hennigan et al., 2011; Heringa et al., 2011; Ortega et al.,
75 2013) and in field campaigns (DeCarlo et al., 2010; Lee et al., 2008; Reid et al., 1998; Yokelson et al.,
76 2009). This SOA can condense onto existing particles causing growth of the aerosol size distribution. It
77 can also spur new-particle formation in biomass-burning plumes as has been observed in lab studies
78 (Hennigan et al., 2012) and field campaign analyses (Vakkari et al., 2014). Conversely, recent lab and
79 field studies have characterized primary organic aerosol (POA) as semi-volatile, with plume dilution
80 allowing the evaporation of organic aerosol from particles (Huffman et al., 2009; Cubison et al., 2011;
81 May et al., 2013, 2015; Jolleys et al., 2015). The cumulative net effects of OA production/loss within
82 biomass-burning plumes has been found to be highly variable from fire to fire (Akagi et al., 2012;
83 Hennigan et. al, 2011).

84 Coagulation is also important for size-distribution evolution as it reduces particle number and
85 shifts the distribution to larger sizes. Coagulation rates are proportional to the square of the particle
86 number concentration (all else remaining fixed), so the high number concentrations in biomass-burning
87 plumes relative to background can lead to rapid coagulation growth of the size distribution. The
88 coagulation rate is therefore also affected by the rate of plume dilution (through a reduction in N), itself
89 a function of plume size and meteorological conditions. The rate and magnitude of the aerosol growth

90 caused by these combined processes is a function of aging time, emission source characteristics,
91 aerosol properties at emission, and atmospheric conditions.

92 These condensation/evaporation and coagulation aging processes affect both the composition and
93 size of the aerosol size distribution – both properties that influence the extent to which smoke particles
94 affect climate. While fresh smoke is generally composed of fine particles between 20-60 nm in
95 diameter (Levin et al., 2010), condensation and coagulation cause rapid aerosol growth to larger sizes
96 (over 100 nm) on timescales of often less than 24 hrs (Janhäll et al., 2010). However, Janhäll et al.,
97 (2010) found the observed geometric mean diameter of aged biomass-burning particles varied between
98 170-300 nm, with geometric standard deviations (hereafter referred to as “modal width”) between 1.3-
99 1.7 with significant dependence on fuel type and modified combustion efficiency. It is currently unclear
100 to what extent these factors and others drive the variability in aged size distributions.

101 As stated earlier, an accurate representation of aged biomass-burning aerosol size is necessary for
102 predictions of aerosol climate effects in regional and global models (Lee et al., 2013). Current wildfire
103 inventories are mass-based (neglecting aerosol size data), and thus regional and global models used for
104 aerosol-climate effects generally specify fixed, “aged” size distributions that do not account for sub-
105 grid processing of the emitted particles (Reid et al., 2009; van der Werf et al., 2010; Wiedinmyer et al.,
106 2011). Any variability in the biomass-burning size distribution due to fire or emissions characteristics
107 and meteorology are not accounted for, nor is it clear what the best “aged” size distribution to use is in
108 these models.

109 In this paper, we perform a detailed investigation of coagulation in biomass-burning plumes and
110 compare to the effects of OA evaporation and formation. We investigate the factors that influence
111 coagulation growth of the particles in the plume. These factors include fire area, particle-emissions
112 mass flux, particle-emissions size, and meteorological conditions. We create parameterizations of
113 varying degrees of complexity for median dry diameter (D_{pm}) and lognormal modal width (σ) of the
114 aged biomass-burning size distributions as a function of these input parameters, based on detailed
115 numerical simulations using a large-eddy model with embedded aerosol microphysics (SAM-TOMAS).
116 Finally, we compare the effect of coagulation on the aerosol size distribution to that of OA
117 production/evaporation.

118 We describe the parameterization building process, including the use of a Gaussian emulator, in
119 Sect. 2. A discussion of input and output ranges, processing, and constraints of the parameters we have

120 chosen is provided in Sect. 2.1. We discuss the SAM-TOMAS model and the emulation process in Sect.
121 2.2-2.3. Sections 3.1-3.2 contain the results of the SAM-TOMAS model and the emulator. We discuss
122 emulator sensitivities to the inputs in Sect. 3.3 and present a series of simplified fit equations for the
123 effective size distributions in Sect. 3.4. We discuss the effects of potential OA production/loss on our
124 size distribution estimates in Sect. 3.5. The simplified-fit equations are tested against biomass-burning
125 plumes observed at the Mt. Bachelor Observatory in Sect. 3.6. Finally, we conclude in Sect. 4,
126 including future plans for testing the parameterization and known existing limitations.

127

128 **2. Methods**

129 Figure 1 provides an overview of our methods that will be described in detail in the subsections below.
130 In short, we used a Large-Eddy Simulation model, the System for Atmospheric Modelling (SAM;
131 Khairoutdinov and Randall, 2003), with the online aerosol microphysics module, Two Moment
132 Aerosol Sectional (TOMAS, Adams and Seinfeld, 2002; Stevens et al., 2012) to simulate the evolution
133 of the biomass-burning aerosol size distribution by coagulation across a wide range of emission and
134 meteorological conditions. We used the SAM-TOMAS size distributions to build parameterizations to
135 predict aged D_{pm} and σ using: (1) a statistical emulator of the SAM-TOMAS model itself and (2)
136 simplified fits to the SAM-TOMAS output data. The statistical emulator was built by the Gaussian
137 Emulation Machine for Sensitivity Analysis (GEM-SA), and we used the emulator and SAM-TOMAS
138 data to determine the relative importance of various inputs to shaping the aged size distribution.

139 ***2.1 Investigated factors that may lead to variability in aged size distributions***

140 We investigated seven parameters that may affect the aging of the biomass-burning aerosol size
141 distribution. These can be divided into those representing the initial lognormal-mode size parameters
142 (D_{pm0} , σ_0), fire conditions (mass flux, fire area), atmospheric conditions (wind speed, plume mixing
143 depth), and time. Each of these parameters is generally available in large-scale aerosol models, which
144 means a parameterization for aged biomass-burning size distributions based on these parameters may
145 be used in these models. Table 1 lists these input parameters and the ranges of values tested in this
146 work.

147 We assumed that the initial size distributions were a single lognormal mode (described by dry
148 median diameter, D_{pm} , and modal width, σ), which is sufficient when representing both fresh and aged
149 observed biomass-burning size distributions (Capes et al., 2008; Janhäll et al., 2010; Levin et al., 2010;
150 Sakamoto et al., 2015). The initial size-distribution parameters specify the median dry diameter (D_{pm0})
151 and modal width (σ_0) of the freshly emitted aerosol distribution. We varied these parameters between
152 20-100 nm for D_{pm0} and 1.2-2.4 for σ_0 . The large ranges are due to variability in combustion efficiency
153 and fuel-type factors as seen in lab and observational studies (Janhäll et al., 2010; Levin et al., 2010).

154 Fire area, mass flux, wind speed and aerosol mixing depth (hereafter referred to as *mixing*
155 *depth*; the vertical extent of the aerosol plume) all affect the aerosol number concentration (N) within
156 the plume, which in turn affects the coagulation rate (proportional to N^2). In our simulations, we
157 constrained mass flux to 2×10^{-8} - 5×10^{-6} kg m⁻² s⁻¹ using approximate maximum and minimum values
158 of summed black carbon and organic carbon flux (BC+OC) found in the Global Fire Emissions
159 Database ver. 3 (GFED3; van der Werf et al., 2010; available from <http://www.globalfiredata.org>). Fire
160 area ranged from 1 - 49 km² (simulated as a square), which was found to represent the range of fire
161 sizes in GFED3. Boundary layer wind speed varied between 2 m s⁻¹ and 20 m s⁻¹ and was based on
162 ranges in the National Center for Environmental Prediction (NCEP) North American Regional
163 Reanalysis (NARR) meteorology (Mesinger et al., 2006) during the fire season (specifically, July,
164 2010). Mixing depth had a range of 150-2500 m (based on SAM-TOMAS output; see Sect. 2.2).

165 The aging time was the final input parameter, and we used 5 hr (300 min) as an upper time
166 bound due to this being a typical timescale for transport across large global model gridboxes.

167 **2.2 The SAM-TOMAS model**

168 We used the SAM-TOMAS model to simulate the evolution of biomass-burning aerosol size
169 distributions due to coagulation across the range of input parameters described above. SAM
170 (Khairoutdinov and Randall, 2003) is a dynamical large-eddy simulation (LES) model, which has
171 previously been used to model emissions plumes (Lonsdale et al., 2012; Stevens et al., 2012; Stevens
172 and Pierce, 2013). We ran the model in Lagrangian 2D mode (Stevens and Pierce, 2013), in which a
173 wall oriented normal to the mean boundary layer wind moves at the mean boundary-layer wind speed.
174 This moving wall tracks the radial dispersion of a plume as it travels downwind (Fig. 2). This 2D mode
175 is computationally efficient compared to the full 3D model with minor differences due to axial plume

176 symmetry (Stevens and Pierce, 2013).

177 The size distributions of the aerosol particles in SAM were simulated using the Two Moment
178 Aerosol Sectional (TOMAS; Adams and Seinfeld, 2002) microphysical scheme embedded into SAM.
179 The algorithm simulated the size distribution across 13 logarithmically spaced size bins spanning 3 nm-
180 1 μm with 2 additional bins spanning 1-10 μm . The aerosol size distribution was tracked via two
181 independent moments for each bin of the size distribution (mass and number). TOMAS calculated
182 coagulation explicitly in each grid cell assuming a Brownian diffusion kernel (Seinfeld and Pandis,
183 2006). Our SAM-TOMAS simulations included only coagulation, and particles were assumed to be a
184 single species (no differentiating between BC and OA). The SAM-TOMAS model had previously been
185 tested against observations in Stevens et al. (2012) and Lonsdale et al. (2012) for power plant plumes.

186 We set background aerosol concentrations to zero as the biomass-burning aerosol
187 concentrations emitted into SAM-TOMAS were orders of magnitude larger than those present in a
188 remote background location, and as such the lack of background aerosol would have had an
189 insignificant effect on the rate of in-plume coagulation processing. In cases where the plume dilutes
190 to similar concentrations to the ambient background, subgrid-plume coagulation schemes are no longer
191 necessary, and grid-resolved coagulation will properly account for coagulation. The biomass-burning
192 aerosol was assumed to have a constant density of 1400 kg m^{-3} as primarily a mix of organic
193 compounds, thus we do not consider how changes in BC/OA composition may affect density and
194 coagulation rates. The hygroscopicity of the aerosol particles was set to zero, allowing no water uptake.
195 This assumption is not true of real world biomass-burning aerosol and has been characterized in other
196 works finding hygroscopicities of fresh ($\kappa=0.02-0.8$; Petters et al., 2009) and aged smoke ($\kappa=0.1-0.3$;
197 Engelhart et al., 2012) with a strong dependence on fuel type. In terms of their effect on the size
198 distribution, a constant κ across all particle sizes has the simple effect of increasing the effective
199 diameter of the particles via water uptake by a scalar factor. This initial increase should only have a
200 relatively minor effect on the final dry D_{pm} or σ of the plume after coagulation processing as the mean
201 coagulation rates are relatively insensitive to the size shifting of a particle population (Seinfeld and
202 Pandis, 2006; Stuart et al., 2013).

203 We ran 100 SAM-TOMAS simulations at 500 m x 500 m horizontal resolution (total cross-wind
204 (y-direction) horizontal extent = 100 km), and constant 40 m vertical resolution (total vertical extent =
205 4 km). This resolution accommodated the chosen plume parameters (see Sect. 2.1). The model was run
206 with a master timestep of 2 seconds (varied internally for accuracy in the coagulation calculation) for a

207 duration of 5 model hours (300 minutes). The output from each SAM-TOMAS simulation was
208 recorded at four different times (400 total time slices across 100 simulations) as the plume progressed
209 along the with-wind (x-direction) axis.

210 The seven inputs to the SAM-TOMAS model were constrained to capture a range of biomass-
211 burning characteristics in realistic scenarios and are summarized in Table 2. The ranges of values used
212 for D_{pm0} , σ_0 , fire area and mass flux are the same as those listed in Table 1. The meteorological fields
213 were supplied by NCEP reanalysis meteorology from over North America (land only, lat: 30° - 70° N,
214 lon: 70° -135° W) during the July 2010 fire season. The SAM-TOMAS wall speed was set equal to the
215 mean boundary layer wind speed from NCEP. We filtered these inputs by requiring wind speed $> 2 \text{ m s}^{-1}$
216 to eliminate stagnation situations over the source. The injection height (lower bound) and injection
217 depth of the aerosol were specified at between 50-1500 m and 500-2000 m respectively. No emission
218 injection parameterization (e.g. Freitas et al., 2007) was used as we were only trying to capture a range
219 of mixing depths for our aging calculation, and the absolute height was relatively unimportant. All the
220 SAM-TOMAS simulation inputs were chosen using semi-random Latin hypercube sampling across the
221 ranges listed above (Lee et al., 2012). The results of the full SAM-TOMAS simulation set are
222 summarized in Sect. 3.1.

223 We calculated the time-dependent mixing depth of the plume from vertical profiles averaged
224 horizontally across the entire simulation wall at each time slice. Figure 3 shows a sample of two
225 vertical profiles from different SAM-TOMAS simulations. The mixing depth was defined as the range
226 of altitudes where the aerosol mass was greater than half of the peak aerosol mass:

227
$$\text{mixing depth} = \Delta_{\text{alt } 50\% \text{ peak aerosol mass}}$$

228 In cases where the plume mixed down to the ground, the lower altitude bound was defined as 0
229 m. Runs with mixing depths greater than 2500 m were excluded to ensure that the plume did not reach
230 the model top. In addition to mixing depth, D_{pm} and σ were calculated for each of the SAM-TOMAS
231 time slices from the first and third integrated moments of the size distribution as detailed by Whitby et
232 al. (1991).

233 We do not address new-particle formation in biomass-burning plumes in this work. In plumes
234 where new-particle formation in biomass-burning plumes occurs, our parameterizations will
235 underestimate the number of particles and overestimate the mean diameter of the plume particles.

236 **2.3 Emulation of the SAM-TOMAS output**

237 As running the full SAM-TOMAS model is too computationally expensive for implementation in
238 global aerosol models, we built an offline emulator of the model for use as a parameterization in these
239 global models. We created the emulator using the Gaussian Emulation Machine for Sensitivity Analysis
240 (GEM-SA) developed by the Centre for Terrestrial Dynamics (<http://www.ctcd.group.shef.ac.uk/gem.html>).
241 The GEM-SA software uses a Gaussian process to design a SAM-TOMAS simulator (the emulator)
242 based on the behavior of the known SAM-TOMAS inputs and outputs (the training data). A complete
243 description of GEM-SA statistics and assumptions can be found in Kennedy and O'Hagan (2001) and
244 Kennedy et al. (2008). A description of its application as an estimator in atmospheric-aerosol modelling
245 can be found in Lee et al. (2011). This software was previously used in sensitivity studies in
246 atmospheric-aerosol (Lee et al., 2011, 2012) and vegetation models (Kennedy et al., 2008).

247 We used 400 data points from the set of 100 SAM-TOMAS simulations to train the emulator.
248 GEM-SA assumes that the outputs are a continuous and differentiable function of the inputs to
249 statistically emulate the model and estimate the SAM-TOMAS output (D_{pm} and σ). We used a new set
250 of completed SAM-TOMAS simulations (624 non-training data points) to test our GEM-SA
251 parameterization for accuracy relative to SAM-TOMAS (see Sect. 3.2-3.3).

252 The GEM-SA parameterization requires seven input parameters: D_{pm0} , σ_0 , mass flux, fire area,
253 wind speed, mixing depth and time, and generates predicted aged D_{pm} and σ as outputs. These
254 estimated D_{pm} and σ describe an aged lognormal aerosol mode incorporating the sub-grid scale
255 coagulation taking place inside concentrated biomass-burning plumes and can be used in
256 global/regional models. We have made the GEM-SA parameterization (emulator Fortran subroutine and
257 input files) available as Supplementary Material.

258 **3. Results**

259 **3.1 SAM-TOMAS simulation output**

260 Figure 4 shows the D_{pm} (panels a and c) and σ (panels b and d) as a function of distance for each of the
261 100 SAM-TOMAS simulations used to train the emulator (Sect. 3.2). The influence of several factors
262 (the distance from the source, emissions mass flux, and fire area) on the final aerosol size distributions

263 is apparent in the output of SAM-TOMAS simulations. Panels a and b are colored by the emissions
264 mass flux, whereas panels c and d are colored by $dM/dxdz$ (kg m^{-2} , the amount of aerosol mass in an
265 infinitesimally thin slice of air perpendicular to the direction of the wind, i.e. mass flux \cdot fire area /
266 wind speed/mixing depth). All simulations showed D_{pm} increasing with distance as coagulation
267 progressed in each plume. The coloring in panel a shows that D_{pm} generally increases more rapidly and
268 to higher values with higher emission fluxes. However, panel c shows that $dM/dxdz$ appears to be a
269 better predictor for the increase of D_{pm} with distance than the emissions flux, and the distance and
270 $dM/dxdz$ capture much of the variability in D_{pm} .

271 Panels b and d show that σ tends to converge with distance as simulations with large initial σ
272 generally decrease with distance more rapidly than simulations with smaller initial σ . This convergence
273 happens slowly relative to the times simulated, so the initial σ have a strong influence even at 200 km.
274 The colors and panels b and d show that σ in high emissions-flux and $dM/dxdz$ cases converge more
275 rapidly than low-emissions cases. However, as opposed to the 1.32 modal-width asymptote in the limit
276 of infinite coagulation found by Lee (1983), the SAM-TOMAS simulations converge to a limit of 1.2-
277 1.25. This is likely due to the size-distribution bin-spacing in the SAM-TOMAS model, where modal
278 widths <1.32 are smaller than a single TOMAS size bin width, which results in less accurate fits of σ
279 for smaller σ values.

280 Figure 5 is a scatterplot of σ vs D_{pm} for each point seen in Fig. 4, excepting those at distances
281 less than 25 km (points close to the emissions source have been removed). The points are colored by
282 $dM/dxdz$. Thus, Fig. 5 shows the results of Fig. 4 panels c and d together but removes the distance
283 information. At these distances over 25 km, D_{pm} is relatively well constrained by $dM/dxdz$ alone,
284 showing that the mean growth by coagulation is strongly influenced by the mass of particles in the slice
285 of air. On the other hand, σ is unconstrained at low values of $dM/dxdz$ but more constrained towards
286 1.2-1.4 at high values of $dM/dxdz$. At high $dM/dxdz$ values, the convergence towards the steady-state σ
287 proceeds much more rapidly than at low $dM/dxdz$ as also shown in Fig. 4d.

288 These SAM-TOMAS results show that $dM/dxdz$ is a powerful determinant of aged biomass-
289 burning size. In these tests, we also explored the suitability of dM/dx (mass flux \cdot fire area/ wind speed)
290 and dM/dV (initial mass concentration). Large mixing depths dilute particle concentrations and reduce
291 coagulation, so we expected that $dM/dxdz$ may be a better predictor of biomass-burning size-
292 distribution aging than dM/dx . However, Fig. 4 and Fig. 5 did not look qualitatively different when
293 using dM/dx or dM/dV . A comparison of dM/dx vs $dM/dxdz$ vs dM/dV in predicting final size-

294 distribution attributes is further discussed in Section 3.4. We quantitatively evaluate the fidelity of
295 dM/dx and $dM/dxdz$ as proxies for biomass-burning size-distribution aging in Sect. 3.4. In the
296 following two subsections, we use the emulator to determine the contribution of the individual inputs to
297 the changes in simulated D_{pm} and σ .

298 ***3.2 Model parameterization evaluation***

299 We tested the GEM-SA-derived emulator parameterization against additional SAM-TOMAS model
300 runs that were not used in the fitting of the parameterization, and we show the results in Fig. 6. We use
301 624 additional SAM-TOMAS-simulated data points that were not used for GEM-SA training in this
302 evaluation. The emulator parameterization-predicted outputs corresponding to these data points for D_{pm}
303 and σ are plotted against the SAM-TOMAS D_{pm} and σ . Predicted D_{pm} has an R^2 value of 0.83 with a
304 slope of 0.92. Larger absolute errors in D_{pm} are found at the larger diameter sizes, but 86% are found
305 within 10% of the SAM-TOMAS D_{pm} (76% of predicted D_{pm} are within 5% of SAM-TOMAS D_{pm}).
306 The small mean normalized bias (MNB) of -0.06 indicates a slight negative bias in the
307 parameterization. This bias is generally seen towards the higher final D_{pm} values in the simulations
308 (>250 nm), which are reached only by the most aged plumes with the heaviest aerosol loads. The σ plot
309 (Fig. 6b) shows a similar correlation coefficient ($R^2=0.91$) and has a slope of 0.93. The MNB is 0.01
310 and 77% of the predicted σ points are within 5% of the σ calculated from SAM-TOMAS. The cluster of
311 points near $\sigma = 1.2-1.3$ is indicative of the modal width steady-state limit. This limit is not captured by
312 the σ parameterization, which assumes a smooth function towards even lower σ values.

313 ***3.3 Sensitivity of aged size distribution to input parameters***

314 Figures 7 and 8 show the sensitivities of the parameterization outputs (D_{pm} and σ , respectively) to the
315 input parameters (D_{pm0} , σ_0 , mass flux, fire area, wind speed, time, and mixing depth) as determined by
316 the GEM-SA emulation of the SAM-TOMAS output. (Note that distance was used as the dependent
317 variable in Fig. 4, while we use time in the emulator. Time can be converted to distance by multiplying
318 by the wind speed). In every panel, each line shows the change in D_{pm} (Fig. 7) or σ (Fig. 8) as an input
319 parameter (e.g. D_{pm0} in panel a) is varied systematically from its minimum to maximum tested value
320 with a randomly chosen set of the other six input parameters. Each panel contains 100 lines, which
321 means that 100 sets of the six other input parameters were randomly chosen to make these lines. We
322 normalize each line by the value of D_{pm} or σ at the midpoint of the x-axis (i.e. where the input

323 parameter is at the midpoint of its tested range). For time since emission (panel f) we normalize by the
324 values at $t=0$ min instead of at the midpoint of the range. These plots therefore show the percent change
325 in D_{pm} or σ , $\Delta\%_{output}$, as each input is changed from its midpoint value (or $t=0$ min for time), in order to
326 emphasize the parameterization's output response to each isolated input variable.

327 The D_{pm} sensitivity plots (Fig. 7) show a number of well-defined responses of D_{pm} to the inputs.
328 D_{pm} increases monotonically with increases in mass flux and fire area (Fig. 5b,d), and decreases nearly
329 monotonically with wind speed. These trends are due to the interrelationships of these inputs with
330 starting number concentration. These results are consistent with Fig. 4 and Fig. 5, where D_{pm} increased
331 with increasing dM/dx in the SAM-TOMAS simulations. Additionally, the D_{pm} also decreases
332 monotonically with mixing depth (albeit more weakly than mass flux, fire area, and wind speed), so
333 $dM/dxdz$ may also be a good proxy for biomass-burning size-distribution aging (evaluated in Sect. 3.4).
334 Higher dM/dx and $dM/dxdz$ values lead to higher initial number concentration in these plumes, which
335 drive higher rates of coagulation due the squared dependence of coagulation rate on number
336 concentrations.

337 D_{pm} also increases nearly monotonically with time (the regions of slight decreases with time
338 show that the parameterization is not necessarily always physically representative due to the statistical
339 nature of the fit over the parameter space). The rapid rise in D_{pm} for time <2 hrs is due to the high
340 number concentrations (N) and coagulation rates near the source. As dilution and coagulation progress,
341 N decreases and coagulation slows, resulting in a slowing of D_{pm} increase. Mass flux has the largest
342 range of output D_{pm} associated with the input ranges specified here ($\sim -50\%$ to $+100\%$).

343 The relationship between D_{pm} and the initial size parameters (D_{pm0} and σ_0) is more complicated.
344 Neither D_{pm0} nor σ_0 show monotonic increases or decreases in D_{pm} due to changes in either of these
345 isolated inputs. In general, there is an increasing trend in output D_{pm} with increasing D_{pm0} , but for some
346 cases it decreases. These decreases in D_{pm} are likely due to (1) decreasing particle number
347 concentrations with increasing D_{pm0} , which leads to reduced coagulation rates and (2) imperfections in
348 the statistical fit of the parameter space. The larger σ_0 indicate broader emission size distributions, with
349 more large particles and small particles. Since coagulation progresses fastest between large and small
350 particles (as opposed to particles of approximately the same size), this favors higher D_{pm} at higher σ .
351 However, the initial particle number decreases with increasing σ , which lowers the coagulation rate and
352 leads to lower D_{pm} .

353 The emulator-derived σ sensitivities are shown in Fig. 8. Since we expect σ to converge towards
 354 an asymptotic limit with coagulation processing (Fig. 4b,d), we see with those input parameters
 355 associated with higher plume number density (mass flux, fire area, wind speed⁻¹, mixing depth⁻¹), which
 356 gave monotonic increases for D_{pm} , show mixed results for σ due to variability in the initial σ_0 . The time
 357 sensitivity plot (Fig. 8f) shows decreasing σ with time similar to Fig. 4b,d.

358 Emission σ_0 shows the most pronounced and largest magnitude effect on output σ (~ -30% to
 359 +30%). Thus, the timescales for σ evolving towards 1.2 is longer than the timescales tested here for
 360 even the densest plumes. These sensitivity plots show that there is less variability in σ than in D_{pm} over
 361 the tested input space.

362 ***3.4 Simplified fits to the aged size distributions***

363 In addition to the GEM-SA emulator fits, we determined simplified fits for both D_{pm} and σ based on the
 364 behavior in Fig. 4 and Fig. 5. These fits are easier to implement in regional and global aerosol models
 365 than the full GEM-derived parameterization. These equations are meant to produce approximate
 366 estimates of D_{pm} and σ throughout plume size-distribution aging. The equations require: the initial
 367 value of the size-parameter of interest (D_{pm0} or σ_0), a value proportional to the plume aerosol loading
 368 ($dM/dxdz$: mass flux · fire area / wind speed / mixing depth or dM/dx : mass flux · fire area / wind
 369 speed), and time since emission from the source fire (time). (Distance may also be used in these
 370 equations rather than time, and distance/wind-speed should be used in place of time.) The functional
 371 forms fitted for D_{pm} and σ are found below.

$$D_{pm} = D_{pm0} + A [dM/dx]^b (\text{time})^c \quad (1)$$

$$D_{pm} = D_{pm0} + A [dM/dxdz]^b (\text{time})^c \quad (2)$$

$$\sigma = \sigma_0 + A [dM/dx]^b (\text{time})^c (1.2 - \sigma_0) \quad (3)$$

$$\sigma = \sigma_0 + A [dM/dxdz]^b (\text{time})^c (1.2 - \sigma_0) \quad (4)$$

372

373 where A, b and c are determined by fitting each equation to the SAM-TOMAS data. For these
 374 empirical equations, the units of dM/dx are kg m^{-1} , $dM/dxdz$ are kg m^{-2} , D_{pm} is nm and time since

375 emission is min. It should be noted that the equations for D_{pm} and σ are designed to be independent of
376 each other (i.e. D_{pm} is not dependent on σ_0), which differs from the GEM-SA emulator. The aerosol
377 loading parameter dM/dx was chosen based on the stratification seen in Fig. 4c and Fig. 5. $dM/dxdz$
378 was tested as well, as it incorporates the variance associated with mixing depth into the fit. The fit to
379 dM/dx rather than $dM/dxdz$ may be advantageous because we expect mixing depth of the plume to be
380 one of the more uncertain parameters in an atmospheric model, and the D_{pm} sensitivities to mixing
381 depth tend to be smaller than those to mass flux, fire area and wind speed in the GEM-SA emulator
382 (Fig. 7). The σ fits introduce a fourth factor, $(1.2-\sigma_0)$, which represents the difference between the
383 SAM-TOMAS infinite-coagulation limit (Fig. 4b and d) and the initial modal width.

384 The scalar A, b and c variables were fit to the ensemble of SAM-TOMAS data. Their values are
385 summarized in Table 3. The fits were tested against independent SAM-TOMAS data in Fig. 9 (D_{pm}) and
386 Fig. 10 (σ). The simplified D_{pm} parameterizations, as expected, are not as good a fit of the SAM-
387 TOMAS data as the GEM-SA emulator (Fig. 6). The fit statistics for the simple parameterizations are
388 as follows: $D_{pm}(dM/dx)$: slope = 0.82, $R^2 = 0.67$, MNB= 0.003, $D_{pm}(dM/dxdz)$: slope = 0.98, $R^2 = 0.77$,
389 MNB= 0.008. The fit using $dM/dxdz$ generally performs better than that with dM/dx . The simple σ fit
390 also did not perform as well as the GEM-SA emulator with fit statistics of: $\sigma(dM/dx)$: slope = 0.64, $R^2 =$
391 0.78, MNB= 0.02 and, $\sigma(dM/dxdz)$: slope = 0.65, $R^2 = 0.79$, MNB= 0.01). Thus, $dM/dxdz$ fits do yield
392 better results than dM/dx (in particular for D_{pm}); however, a user may choose to use the dM/dx fit if the
393 mixing depth is unknown. We note that these fits are only valid within the parameter ranges shown in
394 Table 1. dM/dV was also tested as a parameter within these simplified parameterization, but did not
395 yield better agreements for either D_{pm} or σ than $dM/dxdz$ despite incorporating an additional plume
396 parameter (initial plume y-extent). This is because $dM/dxdz$ is the product of dM/dV and the initial
397 plume width; since wider plumes are less susceptible to dilution than narrower plumes, $dM/dxdz$
398 captures this plume-width effect while dM/dV does not.

399 **3.5 OA production/loss**

400 One of the limitations of the coagulation-only parameterizations derived in this paper is that they do not
401 include the effects of potential condensation/evaporation of organic aerosol on the aged biomass-
402 burning size distribution. Both condensational growth and evaporative loss of OA has been observed
403 previously in chamber studies and the field due to OA production or evaporation from
404 dilution/chemistry (Cubison et al., 2011; Hecobian et al., 2011; Hennigan et al., 2011; Grieshop et al.,

405 2009; Ortega et al., 2013; Jolleys et al., 2015; Vakkari et al., 2014). Konovalov et al. (2015) has
406 emphasized the importance of OA simulation in modeling long-range (>1000 km) plume evolution.
407 Thus, in order to predict biomass-burning aerosol mass, and thus the aerosol size distribution, we must
408 understand how OA evolves in biomass-burning plumes.

409 Here we present a simple correction to our coagulation-only parameterizations to account for
410 in-plume OA production/loss, assuming that this production/loss is known. This correction assumes all
411 SOA condenses onto existing particles (no new-particle formation). Each parameterization presented in
412 this paper may be corrected to include OA production/evaporation using the corrections below. We
413 assume that the OA production or loss does not affect the coagulation rates or σ , but acts to increase the
414 final D_{pm} . These assumptions are imperfect as irreversible condensation (evaporation) decreases
415 (increases) σ ; however, σ is preserved during condensation or evaporation of semi-volatile material
416 (Pierce et al., 2011). Regardless, for the relatively small amounts of OA condensation/evaporation
417 considered here, the change in σ and coagulation rates should be minor. For a factor of 25% growth in
418 diameter from SOA, which may be expected from for a factor of 2 increase in OA mass with a small
419 change in sigma, we expect coagulation rates to stay within about 10% (Seinfeld and Pandis, 2006).
420 For larger changes in OA mass (more than a factor of ~2) due to production/loss, our simple correction
421 will have uncertainties due to these assumptions. Our correction to the final D_{pm} has the following
422 form:

$$D_{pm\ w/OA\ prod/loss} = D_{pm\ w/o\ OA\ prod/loss} \cdot \left(\frac{OAMass_{w/OA\ prod/loss} + BCMass}{OAMass_{w/o\ OA\ prod/loss} + BCMass} \right)^{1/3} \quad (5)$$

423

424 where $D_{pm\ w/o\ OA\ prod/loss}$ is the final D_{pm} from the coagulation-only GEM-SA emulator parameterization,
425 the biomass-burning aerosol OA mass (with and without additional production or loss) is in kg (per
426 particle or volume of air) and the BC mass is in kg (per particle or volume of air). Thus, for a doubling
427 of OA due to SOA production (one of the larger enhancements found in Hennigan et al., 2011),
428 particles that contain negligible BC will grow in diameter by 26% above the coagulation-only
429 predictions. If the particles contained 50% BC, then the diameter growth would only be 14%.

430 While these changes are expected to be on the large end for growth by SOA production, they
431 are significantly smaller than the ~200% variability in aged D_{pm} due to coagulation over the range of
432 initial fire conditions (Fig. 7). For example, variations in wind speed, mass flux, and fire area alone can

433 independently cause variability in the aged D_{pm} by a factor of 2 due to changes in coagulation rates
434 while variability in condensational growth appears to cause much smaller uncertainties (~25%) in the
435 aged D_{pm} . This indicates that although SOA condensational growth is certainly important in shaping
436 particle composition and total particle mass, it is not among the most dominant factors determining the
437 aged D_{pm} compared to those fire-condition parameters controlling coagulation growth. It should be
438 noted, however, that the D_{pm} growth attributed to OA condensation is not accompanied by a change in
439 particle number (additional OA mass is distributed among existing particles), whereas a similar
440 increase in D_{pm} growth by coagulation only would have an accompanying decrease in particle number.
441 Thus, the changes to the aerosol size distribution and climatic influence of a size change due to
442 coagulation and condensation are different.

443 ***3.6 Estimating aged size distributions observed at the Mt. Bachelor Observatory***

444 The simplified fits presented in Section 3.4 (equations 1-4) were tested against size distributions
445 measurements of biomass-burning plumes observed at the Mt. Bachelor Observatory (MBO) in Central
446 Oregon (43.98°N, 121.69°W, 2,764 m a.s.l.). MBO is a mountaintop site that has been in operation
447 since 2004 (Jaffe et al., 2005). An intensive campaign was performed during the summer of 2015 to
448 measure aerosol physical and optical properties of wildfire emissions (Laing et al., in prep). During this
449 campaign aerosol size distributions from 14.1 to 637.8 nm were measured with a Scanning Mobility
450 Particle Sizer (SMPS). Additional details about MBO and the sampling campaign can be found in
451 Laing et al. (in prep).

452 We identified eleven biomass-burning plumes during August (Table 4). Criteria for plume
453 selection was aerosol scattering $> 20 \text{ Mm}^{-1}$ and CO $> 150 \text{ ppbv}$ for at least an hour, a strong correlation
454 ($R^2 > 0.80$) between aerosol scattering and CO, and consistent backward trajectories indicating
455 transport over known fire locations. We calculated back-trajectories to determine fire locations using
456 the National Oceanic and Atmospheric Administration Hybrid Single-Particle Lagrangian Integrated
457 Trajectory (HYSPLIT) model, version 4 (Draxler, 1999; Draxler and Hess, 1997, 1998; Stein et al.,
458 2015) with Global Data Assimilation System (GDAS, $1^\circ \times 1^\circ$) data. The Mt. Bachelor summit is located
459 at ~1500 m amgl (above model ground level), so the back-trajectory starting heights of 1300, 1500, and
460 1700 m amgl were chosen (Ambrose et al., 2011). Fire locations were identified using Moderate
461 Resolution Imaging Spectroradiometer (MODIS) satellite-derived active fire counts
462 (<http://activefiremaps.fs.fed.us/>; Justice et al., 2002).

463 For the plume aerosol loading parameterization inputs in equations 1-4, we used Fire INventory
464 from NCAR (FINN) daily-averaged fire area and fire-emissions estimates (Wiedinmyer et al. 2011).
465 Multiple FINN data points in the same vicinity were combined based on the location of large-wildfire
466 incidents tracked by the National Interagency Fire Center (NIFC) (<http://activefiremaps.fs.fed.us/>). We
467 calculated the mass flux for the aerosol-loading estimates ($dM/dxdz$ and dM/dx) using these FINN
468 OC+BC emissions (kg/day) and FINN fire area data (km^2). Mixing depth was defined as the mixing
469 depth at the source location of the fire in the Global Data Assimilation System (GDAS, $1^\circ \times 1^\circ$) data.
470 Wind speed was also extracted from GDAS data and was calculated as the average wind speed from the
471 ground to the defined mixing height. If no data were available, the mixing height and wind speed were
472 set to 660 m and 8.5 m/s based on the median value of the rest of the plumes. We assumed the emission
473 diameter (D_{pm0}) to be 100 nm, and we calculated σ using initial modal widths (σ_0) of 1.6, 1.9 and 2.4, to
474 be discussed later. We estimated the transport time from plume back-trajectories, and these values
475 ranged from 4.5 to 35 hours.

476 The measured and calculated size distribution diameter and modal widths for each plume at
477 MBO are summarized in Table 4. We calculated D_{pm} and σ as the geometric mean diameter and
478 geometric standard deviation of the plume averaged size distribution as measured by the SMPS,
479 respectively. The plume-averaged size distributions may be influenced by non-biomass-burning
480 particles included along the trajectory from the wildfire. Plumes 1, 2, and 4 have bimodal distributions.
481 The second mode (Aitken mode) of these distributions are an example of influence from a non-biomass
482 burning source. These three bimodal distributions have inflated σ values, which will be addressed later.
483 Due to the large number of fires in Northern California and Oregon during the summer of 2015, some
484 of the plumes observed at MBO were influenced by more than one fire (e.g. Figure 9). For these
485 plumes, we calculated aged D_{pm} and σ values for each fire area (black squares in Figure 9) and a
486 weighted average based on aerosol loading (dM/dx or $dM/dxdz$) was taken. Column 3 in Table 4
487 indicates how many fire areas were averaged for each plume.

488 Figure 10 shows the predicted aged D_{pm} plotted against the observed values for both the dM/dx
489 and $dM/dxdz$ forms of the simple parameterization. An initial D_{pm0} of 100 nm was assumed. Equation 2
490 (using aerosol mass loading $dM/dxdz$) estimates D_{pm} somewhat more accurately ($y = 0.93x + 17.1$, $R^2 =$
491 0.551) than Eqn. 1, which uses aerosol mass loading dM/dx ($y = 0.62x + 53.1$, $R^2 = 0.532$). Over half
492 of the variability in the observed D_{pm} was captured by the simplified fits. Thus, the simple
493 parameterizations show skill at predicting the aged D_{pm} values relative to choosing a constant value of

494 aged D_{pm} as is typically done in regional and global models.

495 Figure 11 shows the predicted aged σ plotted against the observed values for both
496 parameterization forms. Both parameterizations do not predict modal width as well as D_{pm} (Figure 11).
497 The calculated modal width changed significantly when using different emission modal-width values
498 (σ_0). Janhäll et al. (2010) found the σ of fresh biomass burning emissions to range from ~ 1.6 to 1.9 .
499 When using a σ_0 of 1.6 , we underestimated all of the σ values. Using a σ_0 of 1.9 , we improved the
500 estimation of aged σ ranging from 1.4 - 1.6 (Figure 11a). The three higher measured σ values are from
501 the bimodal plumes mentioned previously, which have larger σ values than would be due strictly to the
502 biomass-burning plume. We found that using a σ_0 of 2.4 provided the best fit for all of the measured
503 plumes (Figure 11b), 2.4 being the max σ_0 value from Table 2. The σ simplified fits using $\sigma_0 = 2.4$ have
504 statistics of: $\sigma(dM/dx)$: $y = 0.50 + 1.00x$, $R^2 = 0.513$, and $\sigma(dM/dxdz)$: $y = 0.57 + 0.77x$, $R^2 = 0.468$.
505 Thus, both parameterizations do not predict modal width as well as D_{pm} ; however, these
506 parameterizations do show skill relative to assuming a constant value of σ .

507 The results from the regional fires demonstrate that the parameterizations in Eqs 1-4 can be
508 successfully used to estimate aged biomass-burning size distributions in regional biomass-burning
509 plumes with transport times up to 35 hours with significantly better skill than assuming fixed values for
510 size-distribution parameters. More investigations of individual aged biomass-burning plumes,
511 specifically with one clear source, should be completed to fully characterize this parameterization.

512

513 4. Conclusions

514 We used the SAM-TOMAS large-eddy simulation model and an emulation technique to explore the
515 evolution of biomass-burning aerosol size distributions due to coagulation and build coagulation-only
516 parameterizations of this size-distribution evolution. We have also provided a simple correction to the
517 parameterization for cases with net OA production or loss. We used the SAM-TOMAS model to
518 simulate plume dispersion and aerosol coagulation. The SAM-TOMAS results show that the aged D_{pm}
519 can be largely described by dM/dx and the distance from the source (or time since emission). These
520 results also show that the aged σ moves from σ_0 towards a value of 1.2 at a rate that depends on dM/dx .

521 The GEM-SA program was used to derive a D_{pm} and σ emulator parameterization based on the

522 SAM-TOMAS results. The parameterization requires seven input parameters: emission D_{pm0} , emission
523 σ_0 , mass flux, boundary layer wind speed, fire area, plume mixing depth, and time since emission. The
524 predicted D_{pm} and σ can then be used as effective unimodal biomass-burning size-distribution
525 parameters in regional and global aerosol models.

526 The D_{pm} parameterization showed the strongest sensitivities to those input parameters associated
527 with the extent of aerosol loading within the plume (mass flux, fire area, wind speed). Across the fire
528 area and wind speed ranges tested here, final D_{pm} varied by $\pm 50\%$. Mass flux had the largest associated
529 D_{pm} sensitivity across the tested values (-50% to +100%). These sensitivities were larger than those
530 associated with mixing depth ($\sim -20\%$ to 20%) or the initial size-distribution parameters (D_{pm0} : $\sim -25\%$
531 to 25% , σ_0 : $\sim 15\%$ to -15%). The σ parameterization showed a uniform decrease in σ with time and
532 strong sensitivities to the emission σ_0 (-30% to 30%). This strong sensitivity to σ_0 can be attributed to
533 the inertia in σ evolution in simulations with large modal widths and relatively small mass loading,
534 where σ will not converge quickly to the coagulation limit (1.2).

535 The GEM-SA-derived parameterization performed relatively well against the SAM-TOMAS
536 model with a correlation of $R^2=0.83$, slope of $m=0.92$ and a low mean normalized bias of $MNB=-0.06$
537 for D_{pm} . The σ parameterization has fit statistics of $R^2=0.93$, slope= 0.91 and $MNB=0.01$. The σ
538 parameterization was unable to capture the coagulation limit of 1.2 seen in the SAM-TOMAS results
539 and instead extrapolated to lower values. This 1.2 limit differs from the 1.32 σ limit proposed by Lee
540 (1983) due to the bin-spacing in SAM-TOMAS being coarser than lognormal modes with these small
541 modal widths.

542 We also provided simplified polynomial fits for D_{pm} and σ (Eqns 1-4, Table 3) for calculating
543 aged D_{pm} and σ as independent functions of: the fresh emission parameter (D_{pm0} or σ_0), the mass loading
544 of the aerosol (dM/dx or $dM/dxdz$) and the time since emission from the source fire. The σ fits also
545 require a convergence term to account for the coagulation limit (1.2 in the SAM-TOMAS model).
546 Tested against independent SAM-TOMAS data, the D_{pm} simplified fits performed as: $D_{pm}(dM/dx)$:
547 slope = 0.82, $R^2 = 0.67$, $MNB=0.003$ and $D_{pm}(dM/dxdz)$: slope = 0.98, $R^2 = 0.77$, $MNB=0.008$. The σ
548 simplified fits have statistics of $\sigma(dM/dx)$: slope = 0.64, $R^2=0.78$, $MNB=0.02$ and $\sigma(dM/dxdz)$: slope
549 = 0.65, $R^2 = 0.79$, $MNB=0.01$. The equations requiring ($dM/dxdz$) performed better than their (dM/dx)
550 counterparts as they also account for the aerosol layer depth.

551 We provided a correction for OA production/loss, and showed that significant production of

552 SOA within the plume (~ 100% OA mass enhancement) would cause a relatively small shift in the size-
553 distribution D_{pm} (14-26% increase) compared to other factors that control the coagulation rate (e.g.
554 dM/dx). We note, however, that OA production increases D_{pm} without loss of particle number while
555 coagulation increases D_{pm} with a decrease in number, thus the climatic impact of condensation and
556 coagulation are different. The simplified OA-production/loss correction assumes no change in σ with
557 condensational growth. Further testing should be done with explicit OA production and loss to better
558 quantify the effects of condensation of the size-distribution evolution.

559 We tested the simplified fits for D_{pm} and σ (Eqns 1-4, Table 3) against 11 aged biomass-burning
560 plumes observed at the Mt. Bachelor Observatory in August of 2015. D_{pm} was reasonably calculated
561 using both measures of aerosol loading, dM/dx and $dM/dxdz$ (R^2 values above 0.7 without an outlier).
562 The fit of calculated σ and measured σ depended heavily on the assumed initial modal width, with an
563 assumed σ_0 of 2.4 working best in our case (R^2 values around 0.75 without an outlier). Despite the
564 changes in calculated D_{pm} and σ due to the estimated emission size distribution, the parameterizations
565 captured the differences from plume to plume in regional biomass-burning plumes, which is based on
566 estimated aerosol loading and transport times.

567 Our analysis does not include any cloud processing of the plume particles, i.e. the production of
568 aqueous SOA within activated plume particles is not accounted for in our simple OA mass correction.
569 The production of SOA within droplets could result in additional SOA mass being only added to the
570 larger, activated particles during activation/evaporation cycling. This extra SOA mass would favor
571 increases in the diameters of the larger particles of the size-distribution only, which could create a
572 bimodal size distribution and increase the overall coagulation rates in the plume (more, larger
573 particles coagulate more rapidly with the small-diameter particles).

574 Future work includes (1) more testing of the parameterizations against real world observations
575 of size distribution aging, and (2) incorporating the parameterizations into regional and global aerosol
576 models for further evaluation against regional/global measurements.

577

578 **5. Author Contribution**

579 K.M. Sakamoto, R.G. Stevens, and J.R. Pierce designed the study. K. M. Sakamoto performed the

580 SAM-TOMAS simulations, and created and evaluated the parameterizations. J.R. Laing tested the
581 parameterizations size distributions of aged biomass burning plumes observed at the Mt. Bachelor
582 Observatory, and D.A. Jaffe oversaw the Mt. Bachelor measurements. K. M. Sakamoto prepared the
583 manuscript with assistance from all co-authors.

584 **6. Acknowledgements**

585 NCEP Reanalysis data provided by the NOAA/OAR/ESRL PSD, Boulder, Colorado, USA, from their
586 Web site at <http://www.esrl.noaa.gov/psd/>. K.M. Sakamoto was funded by a [Natural Sciences and](#)
587 [Engineering Research Council of Canada](#) (NSERC) PGS-M Fellowship. The authors gratefully
588 acknowledge the NOAA Air Resources Laboratory (ARL) for the provision of the HYSPLIT transport
589 model used in this publication

590

591 **7. References**

- 592 Adams, P. J. and Seinfeld, J. H.: Predicting global aerosol size distributions in general circulation
593 models, *Journal of Geophysical Research-Atmospheres*, 107, 4310 - 4370, 2002.
- 594 Adler, G., Flores, J. M., Abo Riziq, A., Borrmann, S. and Rudich, Y.: Chemical, physical, and optical
595 evolution of biomass burning aerosols: a case study, *Atmos. Chem. Phys.*, 11(4), 1491–1503,
596 doi:10.5194/acp-11-1491-2011, 2011.
- 597 Akagi, S. K., Craven, J. S., Taylor, J. W., McMeeking, G. R., Yokelson, R. J., Burling, I. R., Urbanski,
598 S. P., Wold, C. E., Seinfeld, J. H., Coe, H., Alvarado, M. J. and Weise, D. R.: Evolution of trace
599 gases and particles emitted by a chaparral fire in California, *Atmos. Chem. Phys.*, 12(3), 1397–
600 1421, doi:10.5194/acp-12-1397-2012, 2012.
- 601 Alonso-Blanco, E., Calvo, A. I., Pont, V., Mallet, M., Fraile, R. and Castro, A. Impact of Biomass
602 Burning on Aerosol Size Distribution, Aerosol Optical Properties and Associated Radiative
603 Forcing, *Aerosol Air Qual. Res.*, 006, 708–724, doi:10.4209/aaqr.2013.05.0163, 2014.
- 604 Ambrose, J.L., Reidmiller, D.R. and Jaffe, D.A.: Causes of High O₃ in the Lower Free Troposphere
605 over the Pacific Northwest as Observed at the Mt. Bachelor Observatory. *Atmos. Environ.*, 45,
606 5302–5315, 2011.
- 607 Andreae, M. O. and Merlet, P.: Emission of trace gases and aerosols from biomass burning, *Global*
608 *Biogeochem. Cycles*, 15(4), 955–966, doi:10.1029/2000GB001382, 2001.
- 609 Boucher, O., Randall, D., Artaxo, P., Bretherton, C., Feingold, G., Forster, P., Kerminen, V.-M., Kondo,
610 Y., Liao, H., Lohmann, U., Rasch, P., Satheesh, S. K., Sherwood, S., Stevens, B. & Zhang, X. Y.
611 in *Climate Change 2013: The Physical Science Basis. Contribution of Working Group I to the*
612 *Fifth Assessment Report of the Intergovernmental Panel on Climate Change* (eds. Stocker, T. F.
613 et al.) (Cambridge University Press, 2013).

614 Capes, G., Johnson, B., McFiggans, G., Williams, P. I., Haywood, J., and Coe, H.: Aging of biomass
615 burning aerosols over West Africa: Aircraft measurements of chemical composition, microphysical
616 properties, and emission ratios, *Journal of Geophysical Research*, 113, D00C15,
617 doi:10.1029/2008JD009845, 2008.

618 Carrico, C. M., Petters, M. D., Kreidenweis, S. M., Sullivan, A. P., McMeeking, G. R., Levin, E. J. T.,
619 Engling, G., Malm, W. C. and Collett, J. L.: Water uptake and chemical composition of fresh
620 aerosols generated in open burning of biomass, *Atmos. Chem. Phys.*, 10(11), 5165–5178,
621 doi:10.5194/acp-10-5165-2010, 2010.

622 Carslaw, K. S., Lee, L. A., Reddington, C. L., Pringle, K. J., Rap, A., Forster, P. M., Mann, G. W.,
623 Spracklen, D. V, Woodhouse, M. T., Regayre, L. A. and Pierce, J. R.: Large contribution of natural
624 aerosols to uncertainty in indirect forcing, *Nature*, 503(7474), 67–71 doi:10.1038/nature12674,
625 2013.

626 Cubison, M. J., Ortega, a. M., Hayes, P. L., Farmer, D. K., Day, D., Lechner, M. J., Brune, W. H., Apel,
627 E., Diskin, G. S., Fisher, J. a., Fuelberg, H. E., Hecobian, a., Knapp, D. J., Mikoviny, T., Riemer,
628 D., Sachse, G. W., Sessions, W., Weber, R. J., Weinheimer, A. J., Wisthaler, a., and Jimenez, J. L.:
629 Effects of aging on organic aerosol from open biomass burning smoke in aircraft and laboratory
630 studies, *Atmospheric Chemistry and Physics*, 11, 12 049-12 064, doi:10.5194/acp-11-12049-2011,
631 2011.

632 DeCarlo, P. F., Ulbrich, I. M., Crouse, J., de Foy, B., Dunlea, E. J., Aiken, A. C., Knapp, D.,
633 Weinheimer, A. J., Campos, T., Wennberg, P. O. and Jimenez, J. L.: Investigation of the sources
634 and processing of organic aerosol over the Central Mexican Plateau from aircraft measurements
635 during MILAGRO, *Atmos. Chem. Phys.*, 10(12), 5257–5280, doi:10.5194/acp-10-5257-2010,
636 2010.

637 Draxler, R.R.: HYSPLIT_4 User's Guide, NOAA Technical Memorandum ERL ARL-230, June, 35 pp.,
638 1999.

639 Draxler, R.R., and Hess, G.D.: [An overview of the HYSPLIT_4 modelling system for trajectories,
640 dispersion, and deposition](#). *Australian Meteorological Magazine*, 47: 295-308, 1998.

641 Draxler, R.R., and Hess, G.D.: [Description of the HYSPLIT_4 modeling system](#). NOAA Technical
642 Memo ERL ARL-224, December, 24 p., 1997.

643 Engelhart, G. J., Hennigan, C. J., Miracolo, M. A., Robinson, A. L. and Pandis, S. N.: Cloud
644 condensation nuclei activity of fresh primary and aged biomass burning aerosol, *Atmos. Chem.
645 Phys.*, 12(15), 7285–7293, doi:10.5194/acp-12-7285-2012, 2012.

646 Freitas, S. R., Longo, K. M., Chatfield, R., Latham, D., Dias, M. A. F. S., Andreae, M. O., Prins, E.,
647 and Unesp, F. E. G.: Including the sub-grid scale plume rise of vegetation fires in low resolution
648 atmospheric transport models, *Atmospheric Chemistry and Physics*, pp. 3385 - 3398, 2007.

649 Grieshop, A. P., Logue, J. M., Donahue, N. M. and Robinson, A. L.: Laboratory investigation of
650 photochemical oxidation of organic aerosol from wood fires 1: measurement and simulation of
651 organic aerosol evolution, *Atmos. Chem. Phys.*, 9(4), 1263–1277, doi:10.5194/acp-9-1263-2009,
652 2009.

653 Haywood, J. and Boucher, O.: Estimates of the direct and indirect radiative forcing due to tropospheric
654 aerosols: a review, *Rev. Geophys.*, 38, 513–543, doi:10.1029/1999RG000078, 2000.

655 Hecobian, A., Liu, Z., Hennigan, C. J., Huey, L. G., Jimenez, J. L., Cubison, M. J., Vay, S., Diskin, G.
656 S., Sachse, G. W., Wisthaler, A., Mikoviny, T., Weinheimer, A. J., Liao, J., Knapp, D. J.,

657 Wennberg, P. O., Kürten, A., Crouse, J. D., Clair, J. St., Wang, Y. and Weber, R. J.: Comparison
658 of chemical characteristics of 495 biomass burning plumes intercepted by the NASA DC-8 aircraft
659 during the ARCTAS/CARB-2008 field campaign, *Atmos. Chem. Phys.*, 11(24), 13325–13337,
660 doi:10.5194/acp-11-13325-2011, 2011.

661 Hennigan, C. J., Miracolo, M. A., Engelhart, G. J., May, A. A., Presto, A. A., Lee, T., Sullivan, A. P.,
662 McMeeking, G. R., Coe, H., Wold, C. E., Hao, W.-M., Gilman, J. B., Kuster, W. C., de Gouw, J.,
663 Schichtel, B. A., Kreidenweis, S. M. and Robinson, A. L.: Chemical and physical transformations
664 of organic aerosol from the photo-oxidation of open biomass burning emissions in an
665 environmental chamber, *Atmos. Chem. Phys.*, 11(15), 7669–7686, doi:10.5194/acp-11-7669-2011,
666 2011.

667 Hennigan, C. J., Westervelt, D. M., Riipinen, I., Engelhart, G. J., Lee, T., Collett, J. L., Pandis, S. N.,
668 Adams, P. J. and Robinson, A. L.: New particle formation and growth in biomass burning plumes:
669 An important source of cloud condensation nuclei, *Geophys. Res. Lett.*, 39(9), n/a–n/a,
670 doi:10.1029/2012GL050930, 2012.

671 Heringa, M. F., DeCarlo, P. F., Chirico, R., Tritscher, T., Dommen, J., Weingartner, E., Richter, R.,
672 Wehrle, G., Prévôt, A. S. H. and Baltensperger, U.: Investigations of primary and secondary
673 particulate matter of different wood combustion appliances with a high-resolution time-of-flight
674 aerosol mass spectrometer, *Atmos. Chem. Phys.*, 11(12), 5945–5957, doi:10.5194/acp-11-5945-
675 2011, 2011.

676 Hobbs, P. V., Sinha, P., Yokelson, R. J., Christian, T. J., Blake, D. R., Gao, S., Kirchstetter, T. W.,
677 Novakov, T. and Pilewskie, P.: Evolution of gases and particles from a savanna fire in South
678 Africa, *J. Geophys. Res.*, 108(D13), doi:10.1029/2002JD002352, 2003.

679 Hosseini, S., Li, Q., Cocker, D., Weise, D., Miller, A., Shrivastava, M., Miller, J. W., Mahalingam, S.,
680 Princevac, M. and Jung, H.: Particle size distributions from laboratory-scale biomass fires using
681 fast response instruments, *Atmos. Chem. Phys.*, 10(16), 8065–8076, doi:10.5194/acp-10-8065-
682 2010, 2010.

683 Huffman, J. A., Docherty, K. S., Mohr, C., Cubison, M. J., Ulbrich, I. M., Ziemann, P. J., Onasch, T. B.
684 and Jimenez, J. L.: Chemically-Resolved Volatility Measurements of Organic Aerosol from
685 Different Sources, *Environ. Sci. Technol.*, 43(14), 5351–5357, doi:10.1021/es803539d, 2009.

686 Jacobson, M. Z.: Strong radiative heating due to the mixing state of black carbon in atmospheric
687 aerosols, *Nature*, 409(6821), 695–697, 2001.

688 Jaffe, D., Prestbo, E., Swartzendruber, P., Weissenzias, P., Kato, S., Takami, a, Hatakeyama, S. and
689 Kajii, Y.: Export of atmospheric mercury from Asia, *Atmos. Environ.*, 39(17), 3029–3038,
690 doi:10.1016/j.atmosenv.2005.01.030, 2005.

691 Janhäll, S., Andreae, M. O. and Pöschl, U.: Biomass burning aerosol emissions from vegetation fires :
692 particle number and mass emission factors and size distributions, *Atmos. Chem. Phys.*, 1427–1439,
693 2010.

694 Jolleys, M. D., Coe, H., Mcfiggans, G., Taylor, J. W., Shea, S. J. O., Breton, M. Le, Bauguitte, S. J.,
695 Moller, S., Carlo, P. Di, Aruffo, E., Palmer, P. I., Lee, J. D., Percival, C. J. and Gallagher, M. W.:
696 Properties and evolution of biomass burning organic aerosol from Canadian boreal forest fires, ,
697 3077–3095, doi:10.5194/acp-15-3077-2015, 2015.

698 Justice, C. ., Giglio, L., Korontzi, S., Owens, J., Morisette, J. ., Roy, D., Descloitres, J., Alleaume, S.,
699 Petitcolin, F. and Kaufman, Y.: The MODIS fire products, *Remote Sens. Environ.*, 83(1-2), 244–

700 262, doi:10.1016/S0034-4257(02)00076-7, 2002.

701 Kennedy, M. and O'Hagan, A.: Bayesian calibration of computer models, *J. R. Stat. Soc. Ser. B Stat.*
702 *Methodol.*, 63, 425 - 464, 2001.

703 Kennedy, M., Anderson, C., O'Hagan, A., Lomas, M., Woodward, I., Gosling, J. P., and Heinemeyer, A.:
704 Quantifying uncertainty in the biospheric carbon flux for England and Wales, *Journal of the Royal*
705 *Statistical Society: Series A (Statistics in Society)*, 171, 109-135, doi:10.1111/j.1467-
706 985X.2007.00489.x, 2008.

707 Khairoutdinov, M. F. and Randall, D. A.: Cloud resolving modeling of the ARM summer 1997 IOP:
708 Model formulation, results, uncertainties, and sensitivities, *Journal of the Atmospheric Sciences*,
709 60, 607-625, 2003.

710 Kononov, I. B., Beekmann, M., Berezin, E. V., Petetin, H., Mielonen, T., Kuznetsova, I. N. and
711 Andreae, M. O.: The role of semi-volatile organic compounds in the mesoscale evolution of
712 biomass burning aerosol : a modeling case study of the 2010 mega-fire event in Russia, , 13269–
713 13297, doi:10.5194/acp-15-13269-2015, 2015.

714 Laing, J.R., J. Hee, and D.A. Jaffe. Physical and Optical Properties of Aged Biomass Burning Aerosol
715 during an Exceptional Forest Fire Year in the Pacific Northwest. In Preparation.

716 Lee, K.: Change of particle size distribution during Brownian coagulation, *Journal of Colloid and*
717 *Interface Science*, 92, 315 - 325, doi:http://dx.doi.org/10.1016/0021-9797(83)90153-4, 1983.

718 Lee, L. A., Carslaw, K. S., Pringle, K. J., Mann, G. W., and Spracklen, D. V.: Emulation of a complex
719 global aerosol model to quantify sensitivity to uncertain parameters, *Atmospheric Chemistry and*
720 *Physics*, 11, 12 253{12 273, doi:10.5194/acp-11-12253-2011, 2011.

721 Lee, L. A., Carslaw, K. S., Pringle, K. J., and Mann, G. W.: Mapping the uncertainty in global CCN
722 using emulation, *Atmospheric Chemistry and Physics*, 12, 9739 – 9751, doi:10.5194/acp-12-9739-
723 2012, 2012.

724 Lee, L. A., Pringle, K. J., Reddington, C. L., Mann, G. W., Stier, P., Spracklen, D. V., Pierce, J. R., and
725 Carslaw, K. S.: The magnitude and causes of uncertainty in global model simulations of cloud
726 condensation nuclei, *Atmospheric Chemistry and Physics*, 13, 8879-8914, doi:10.5194/acp-13-
727 8879-2013, 2013.

728 Levin, E. J. T., McMeeking, G. R., Carrico, C. M., Mack, L. E., Kreidenweis, S. M., Wold, C. E.,
729 Moosmüller, H., Arnott, W. P., Hao, W. M., Collett, J. L. and Malm, W. C.: Biomass burning
730 smoke aerosol properties measured during Fire Laboratory at Missoula Experiments (FLAME), *J.*
731 *Geophys. Res.*, 115(D18), D18210, doi:10.1029/2009JD013601, 2010.

732 Lonsdale, C. R., Stevens, R. G., Brock, C. a., Makar, P. a., Knipping, E. M., and Pierce, J. R.: The
733 effect of coal-powered power-plant SO₂ and NO_x control technologies on aerosol nucleation in the
734 source plumes, *Atmospheric Chemistry and Physics*, 12, 11 519-11 531, doi:10.5194/acp-12-
735 11519-2012, 2012.

736 May, A. A., Levin, E. J. T., Hennigan, C. J., Riipinen, I., Lee, T., Collett, J. L., Jimenez, J. L.,
737 Kreidenweis, S. M. and Robinson, A. L.: Gas-particle partitioning of primary organic aerosol
738 emissions: 3. Biomass burning, *J. Geophys. Res. Atmos.*, 118(19), 11,327–11,338,
739 doi:10.1002/jgrd.50828, 2013.

740 May, A. A., Lee, T., Mcmeeking, G. R., Akagi, S., Sullivan, A. P., Urbanski, S. and Yokelson, R. J.:
741 Observations and analysis of organic aerosol evolution in some, , 6323–6335, doi:10.5194/acp-15-
742 6323-2015, 2015.

743 Mesinger, F., Dimego, G., Kalnay, E., Mitchell, K., Shafran, P. C., Ebisuzaki, W., Joviæ, D., Woollen,
744 J., Rogers, E., Berbery, E. H., Ek, M. B., Fan, Y., Grumbine, R., Higgins, W., Li, H., Lin, Y.,
745 Manikin, G., Parrish, D., and Shi, W.: North American Regional Reanalysis: A long-term,
746 consistent, high-resolution climate dataset for the North American domain, as a major
747 improvement upon the earlier global reanalysis datasets in both resolution and accuracy, *B. Am.*
748 *Meteorol. Soc.*, 87, 343–360, 2006.

749 Okoshi, R., Rasheed, A., Chen Reddy, G., McCrowey, C. J. and Curtis, D. B.: Size and mass
750 distributions of ground-level sub-micrometer biomass burning aerosol from small wildfires,
751 *Atmos. Environ.*, 89, 392–402, doi:10.1016/j.atmosenv.2014.01.024, 2014.

752 Ortega, A. M., Day, D. A., Cubison, M. J., Brune, W. H., Bon, D., de Gouw, J. A. and Jimenez, J. L.:
753 Secondary organic aerosol formation and primary organic aerosol oxidation from biomass-burning
754 smoke in a flow reactor during FLAME-3, *Atmos. Chem. Phys.*, 13(22), 11551–11571,
755 doi:10.5194/acp-13-11551-2013, 2013.

756 Petters, M. D. and Kreidenweis, S. M.: A single parameter representation of hygroscopic growth and
757 cloud condensation nucleus activity, *Atmos. Chem. Phys.*, 7(8), 1961–1971, doi:10.5194/acp-7-
758 1961-2007, 2007.

759 Petters, M. D., Carrico, C. M., Kreidenweis, S. M., Prenni, A. J., DeMott, P. J., Collett, J. L. and
760 Moosmüller, H.: Cloud condensation nucleation activity of biomass burning aerosol, *J. Geophys.*
761 *Res.*, 114(D22), D22205, doi:10.1029/2009JD012353, 2009.

762 Pierce, J. R., Chen, K. and Adams, P. J.: Contribution of primary carbonaceous aerosol to cloud
763 condensation nuclei: processes and uncertainties evaluated with a global aerosol microphysics
764 model, *Atmos. Chem. Phys.*, 7, 5447–5466, 2007.

765 Pierce, J.R., Riipinen, I., Kulmala, M., Ehn, Petaja, T., Junninen, H., Worsnop, D.R., Donahue, N.M.:
766 Quantification of the volatility of secondary organic compounds in ultrafine particles during
767 nucleation events, *Atmospheric Chemistry and Physics*, 11, 9019-9036, doi:10.5194/acp-11-9019-
768 2011, 2011.

769 Reid, J. S., Koppmann, R., Eck, T. F. and Eleuterio, D. P.: A review of biomass burning emissions part
770 II: intensive physical properties of biomass burning particles, *Atmos. Chem. Phys.*, 5(3), 799–825,
771 doi:10.5194/acp-5-799-2005, 2005.

772 Rissler, J., Vestin, A., Swietlicki, E., Fisch, G., Zhou, J., Artaxo, P. and Andreae, M. O.: Size
773 distribution and hygroscopic properties of aerosol particles from dry-season biomass burning in
774 Amazonia, *Atmos. Chem. Phys.*, 6, 471–491, 2006.

775 Sakamoto, K. M., Allan, J. D., Coe, H., Taylor, J. W., Duck, T. J., and Pierce, J. R.: Aged boreal
776 biomass-burning aerosol size distributions from BORTAS 2011, *Atmos. Chem. Phys.*, 15, 1633-
777 1646, doi:10.5194/acp-15-1633-2015, 2015.

778 Seinfeld, J. H. and Pandis, S. N.: *Atmospheric Chemistry and Physics*, Wiley, 2006.

779 Spracklen, D. V., Carslaw, K. S., Pöschl, U., Rap, A. and Forster, P. M.: Global cloud condensation
780 nuclei influenced by carbonaceous combustion aerosol, *Atmos. Chem. Phys.*, 11(17), 9067–9087,
781 doi:10.5194/acp-11-9067-2011, 2011.

782 Stein, A. F., Draxler, R. R., Rolph, G. D., Stunder, B. J. B., Cohen, M. D. and Ngan, F.: NOAA’s
783 HYSPLIT Atmospheric Transport and Dispersion Modeling System, *Bull. Am. Meteorol. Soc.*,
784 96(12), 2059–2077, doi:10.1175/BAMS-D-14-00110.1, 2015.

785 Stevens, R. G. and Pierce, J. R.: A parameterization of sub-grid particle formation in sulfur-rich plumes

786 for global- and regional-scale models, *Atmospheric Chemistry and Physics*, 13, 12 117-12 133,
787 doi:10.5194/acp-13-12117-2013, 2013.

788 Stevens, R. G. and Pierce, J. R.: The contribution of plume-scale nucleation to global and regional
789 aerosol and CCN concentrations: evaluation and sensitivity to emissions changes, *Atmospheric*
790 *Chemistry and Physics Discussions*, 14, 21 473 - 21 521, doi:10.5194/acpd-14-21473-2014, 2014.

791 Stevens, R. G., Pierce, J. R., Brock, C. A., Reed, M. K., Crawford, J. H., Holloway, J. S., Ryerson, T.
792 B., Huey, L. G., and Nowak, J. B.: Nucleation and growth of sulfate aerosol in coal-powered
793 power plant plumes: sensitivity to background aerosol and meteorology, *Atmospheric Chemistry*
794 *and Physics*, 12, 189 - 206, doi:10.5194/acp-12-189-2012, 2012.

795 Stuart, G. S., Stevens, R. G., a. I. Partanen, Jenkins, a. K. L., Korhonen, H., Forster, P. M., Spracklen,
796 D. V., and Pierce, J. R.: Reduced efficacy of marine cloud brightening geoengineering due to in-
797 plume aerosol coagulation: parameterization and global implications, *Atmospheric Chemistry and*
798 *Physics*, 13, 10 385-10 396, doi:10.5194/acp-13-10385-2013, 2013.

799 Vakkari, V., Veli-Matti, K., Beukes, J.P., Tiitta, P., van Zyl, P.G., Josipovic, M., Venter, A.D., Jaars, K.,
800 Worsnop, D.R., Kulmala, M. and Laakso, L.: Rapid changes in biomass burning aerosols by
801 atmospheric oxidation, *Geophys. Res. Lett.*, 2644–2651, doi:10.1002/2014GL059396, 2014.

802 Van der Werf, G. R., Randerson, J. T., Giglio, L., Collatz, G. J., Mu, M., Kasibhatla, P. S., Morton, D.
803 C., DeFries, R. S., Jin, Y. and van Leeuwen, T. T.: Global fire emissions and the contribution of
804 deforestation, savanna, forest, agricultural, and peat fires (1997–2009), *Atmos. Chem. Phys.*,
805 10(23), 11707–11735, doi:10.5194/acp-10-11707-2010, 2010.

806 Whitby, E., McMurry, P., Shankar, U., and Binkowski, F. S.: *Modal Aerosol Dynamics Modeling*, Tech.
807 rep., Office of research and development U.S. environmental protection agency, 1991.

808 Wiedinmyer, C., Akagi, S. K., Yokelson, R. J., Emmons, L. K., Al-Saadi, J. A., Orlando, J. J. and Soja,
809 A. J.: The Fire INventory from NCAR (FINN): a high resolution global model to estimate the
810 emissions from open burning, *Geosci. Model Dev.*, 4(3), 625–641, doi:10.5194/gmd-4-625-2011,
811 2011.

812 Yokelson, R. J., Crounse, J. D., Decarlo, P. F., Karl, T., Urbanski, S., Atlas, E., Campos, T. and
813 Shinozuka, Y.: Emissions from biomass burning in the Yucatan, *Atmos. Chem. Phys.*, 5785–5812,
814 2009.

815

816

Table 1. Parameter ranges for each of the seven input parameters investigated in this study.

Parameter	Description	Units	Min. Value	Max. Value
D_{pm0}	Emission median dry diameter	nm	20	100
σ_0	Emission modal width	-	1.2	2.4
Mass Flux	Emission mass flux from fire	$\text{kg m}^{-2} \text{s}^{-1}$	2×10^{-8}	5×10^{-6}
Fire area	Square fire emissions area	km^2	1	49
Wind speed	Mean boundary-layer wind speed	m s^{-1}	2	20
Mixing depth	Mixing depth of aerosol layer	m	150	2500
Time	Time since emission	min	0	300

Table 2. Parameter ranges for inputs to the SAM-TOMAS model.

Parameter	Description	Units	Min. value	Max. value
Date	Req. for Met. field selection	8-hour	July 1, 2010	July 31, 2010
Latitude		deg N	30	70
Longitude		deg W	70	135
D_{pm0}	Emission median dry diameter	nm	20	100
σ_0	Emission modal width	-	1.2	2.4
Mass Flux	Emission mass flux from fire	$\text{kg m}^{-2} \text{s}^{-1}$	2×10^{-8}	5×10^{-6}
Fire area	Square fire emissions area	km^2	1	49
Injection height	Lower plume injection bound	m	50	150
Injection depth	Depth of plume at emission	m	500	2000

Table 3. Best-fit parameters for the simplified D_{pm} and σ SAM-TOMAS parameterizations (Eqns. 1 to 4)

Fit	Eqn. #	Parameter		
		A	b	c
$D_{pm}(dM/dx)$	(1)	4.268	0.3854	0.4915
$D_{pm}(dM/dxdz)$	(2)	84.58	0.4191	0.4870
$\sigma(dM/dx)$	(3)	0.05940	0.1915	0.3569
$\sigma(dM/dxdz)$	(4)	0.2390	0.1889	0.3540

Table 4: Measured and calculated D_{pm} and σ of biomass-burning plumes observed at MBO during August 2015. For the calculated D_{pm} and σ of, the initial size parameters used were $D_{pm0} = 100$ nm and $\sigma_0 = 1.9$.

Plume	Plume date and time (UTC)	# fire areas	Measured (SMPS)		Calculated			
			D_{pm} (nm)	σ	using dM/dx		using $dM/dxdz$	
			D_{pm} (nm)	σ	D_{pm} (nm)	σ	D_{pm} (nm)	σ
1	8/9/2015 3:00-4:00	3	136.1	1.95	140.7	1.64	151.1	1.59
2	8/9/2015 5:00-7:00	3	144.0	1.77	140.8	1.64	152.0	1.58
3	8/10/2015 3:00-5:00	3	190.1	1.50	140.9	1.63	149.7	1.58
4	8/23/2015 3:55-7:00	1	162.5	1.89	145.5	1.63	162.4	1.57
5	8/24/2015 4:00-7:25	1	201.1	1.59	167.5	1.55	184.7	1.49
6	8/24/2015 7:30-11:20	1	217.5	1.52	190.1	1.50	230.1	1.40
7	8/24/2015 13:00-18:00	1	212.5	1.49	193.9	1.48	237.8	1.37
8	8/25/2015 3:50-6:50	1	192.2	1.54	161.4	1.57	172.6	1.52
9	8/27/2015 9:00-13:00	3	192.9	1.50	194.2	1.49	220.6	1.43
10	8/28/2015 8:00-11:15	3	183.4	1.54	182.1	1.50	203.2	1.43
11	8/28/2015 17:40-19:40	3	176.7	1.60	181.4	1.50	202.0	1.43

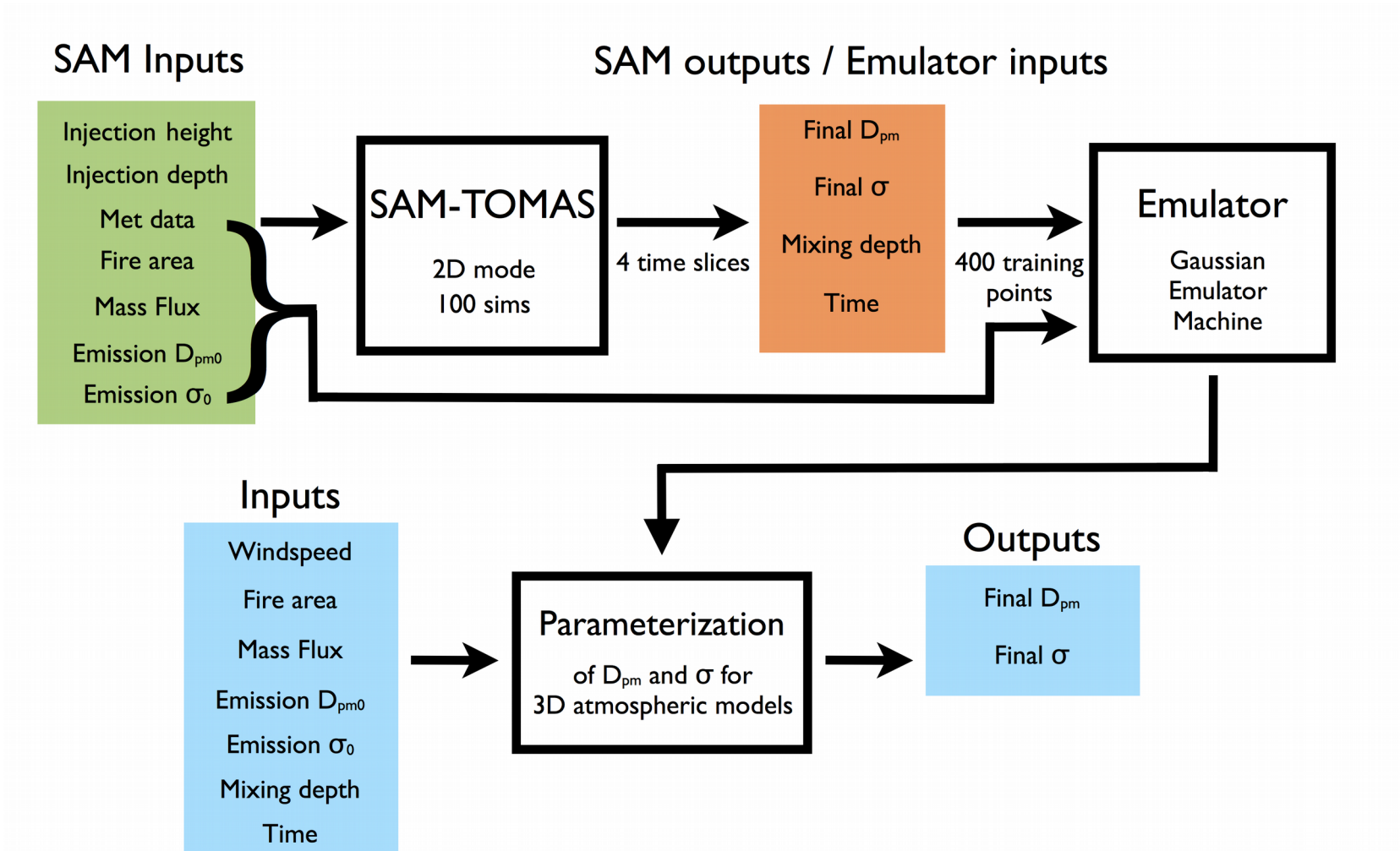


Figure 1. Schematic of the methods in this paper.

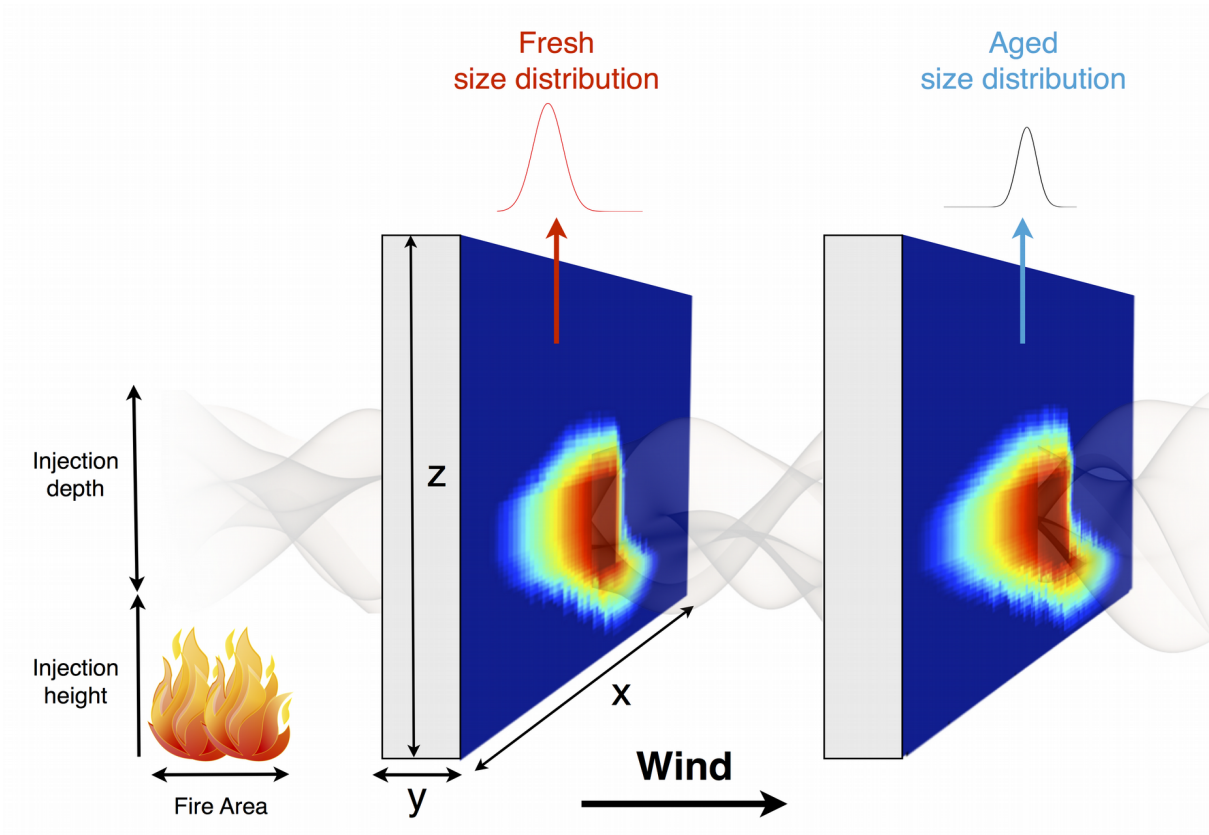


Figure 2. Schematic of a 2D SAM-TOMAS plume simulation.

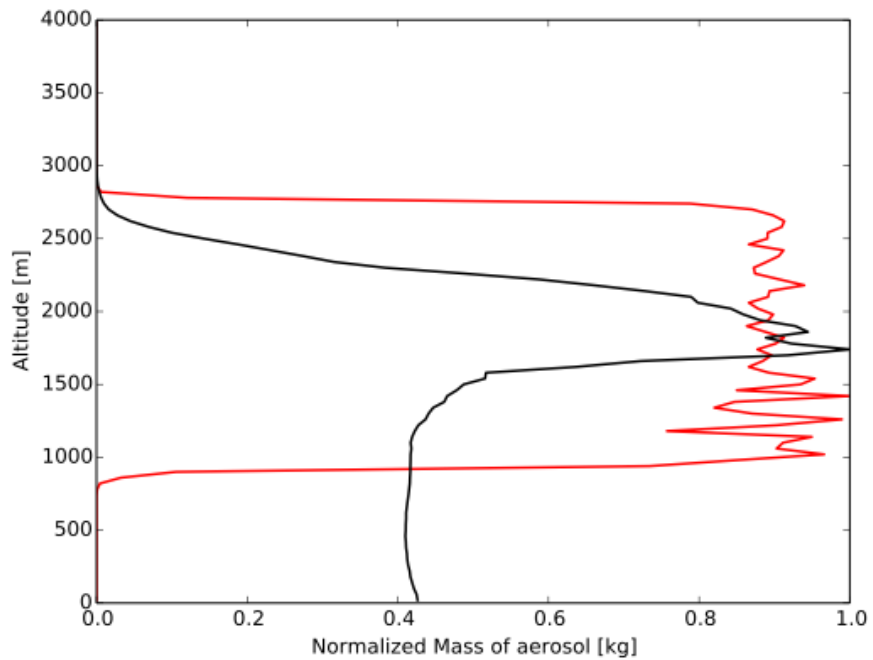


Figure 3. Final vertical profiles for two representative SAM-TOMAS simulations after four hours, normalized to individual aerosol load and averaged horizontally across the domain. The black profile shows a simulation where the aerosol mixed through the boundary layer to the ground with some aerosol still trapped in a stable emission layer, while the red profile shows a simulation where the aerosol plume is still stable at the emission injection layer.

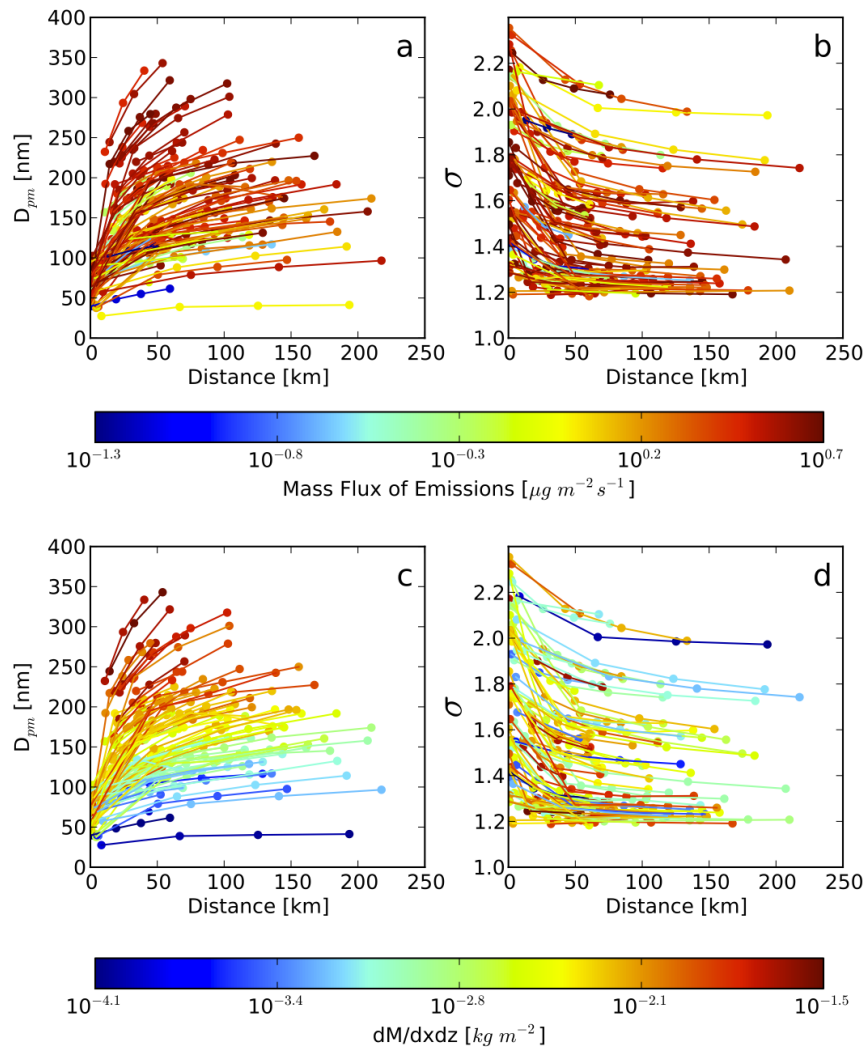


Figure 4. Wire plots showing size-distribution changes across individual SAM-TOMAS simulations colored by emission mass flux (panels a and b) and $dM/dxdz$ (panels c and d) for D_{pm} (panels a and c) and σ (panels b and d).

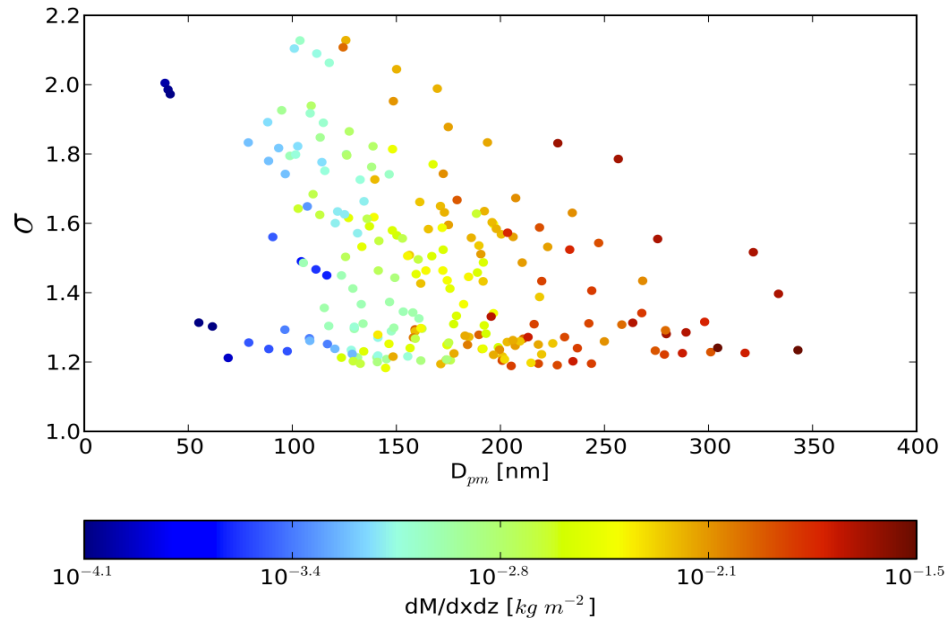


Figure 5. Scatter plot showing the relationships between final modal width (σ), final D_{pm} , and $dM/dxdz$ for each of the SAM-TOMAS simulation slices at distances greater than 25 km from the fire.

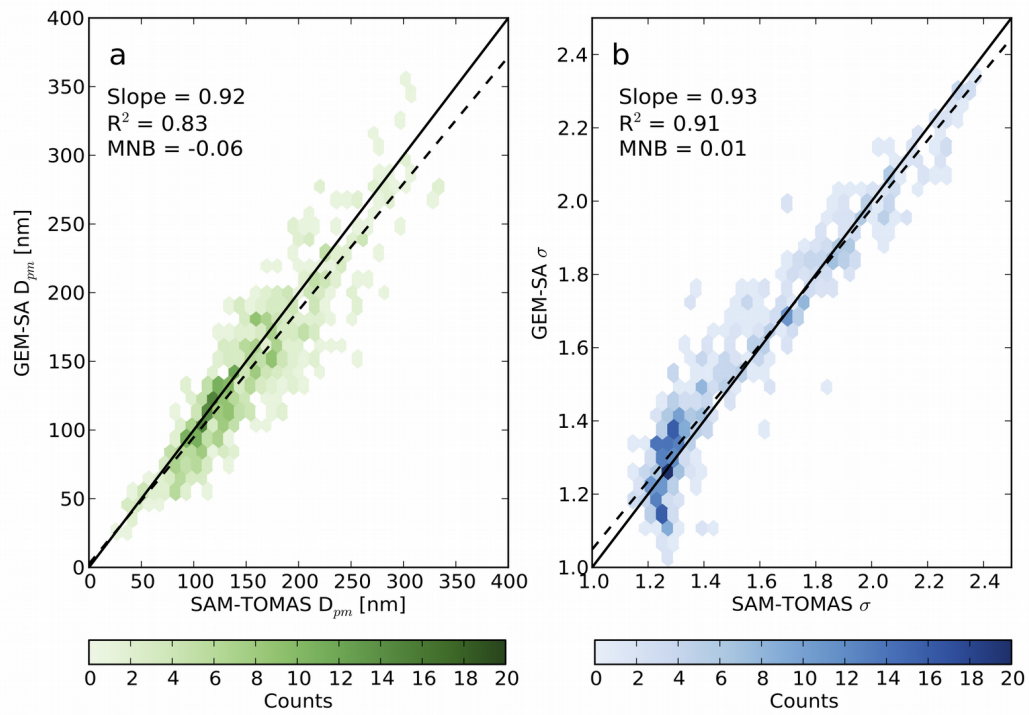


Figure 6. One-to-one plots showing GEM-SA emulator vs. SAM-TOMAS for 624 non-training simulation slices for a) final D_{pm} , and b) final modal width, σ . The black line is the one-to-one line. The dashed black line is the line of best fit.

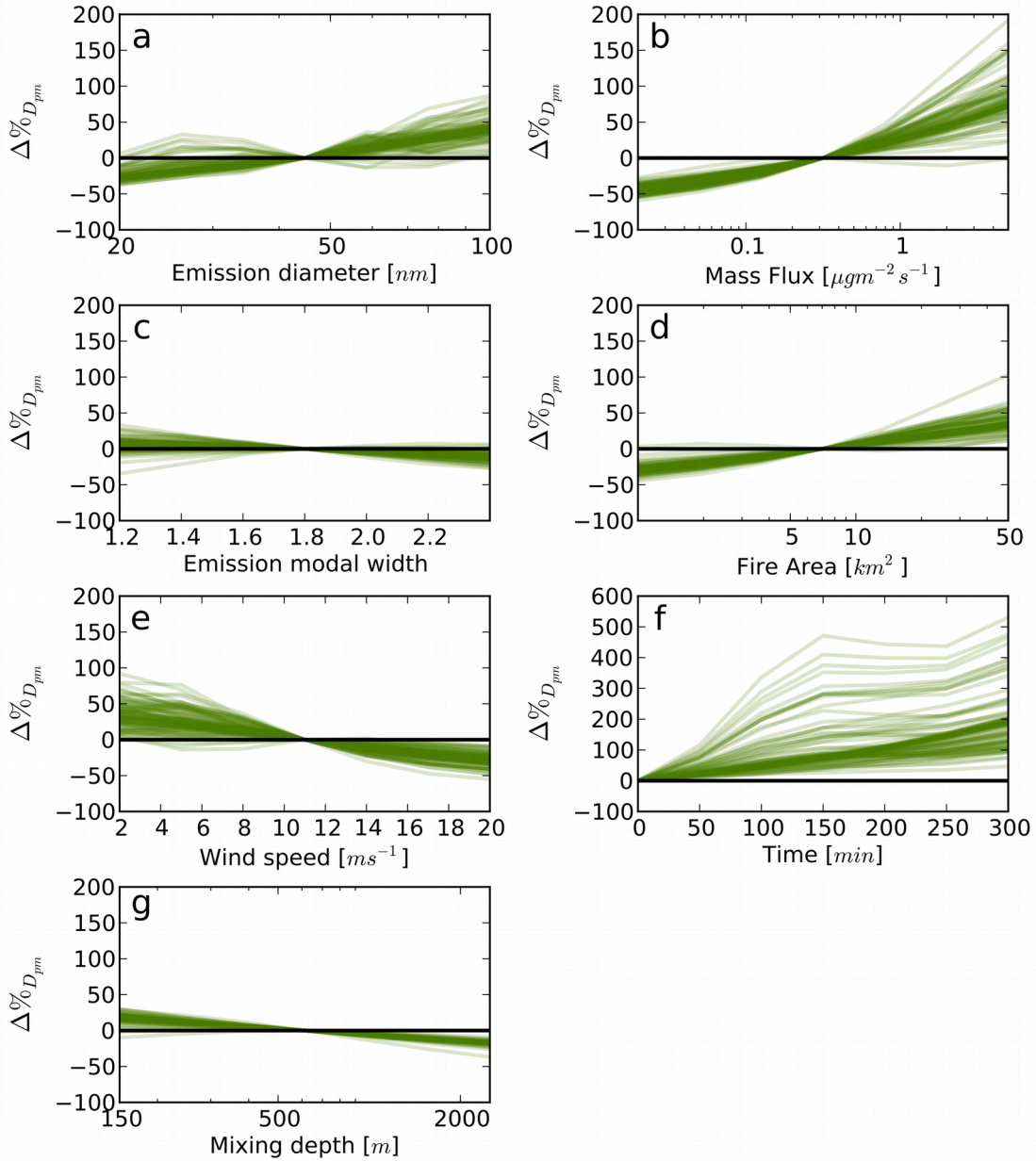


Figure 7. Sensitivity plots for the seven input parameters to the GEM-SA D_{pm} parameterization. For each panel, a single input parameter is varied systematically from its minimum to maximum value for 100 randomly chosen sets of the other six parameters (100 lines in each panel). The sensitivities are shown as percent change in final D_{pm} , individually normalized to the value at the center of the x-axis (to zero in Time).

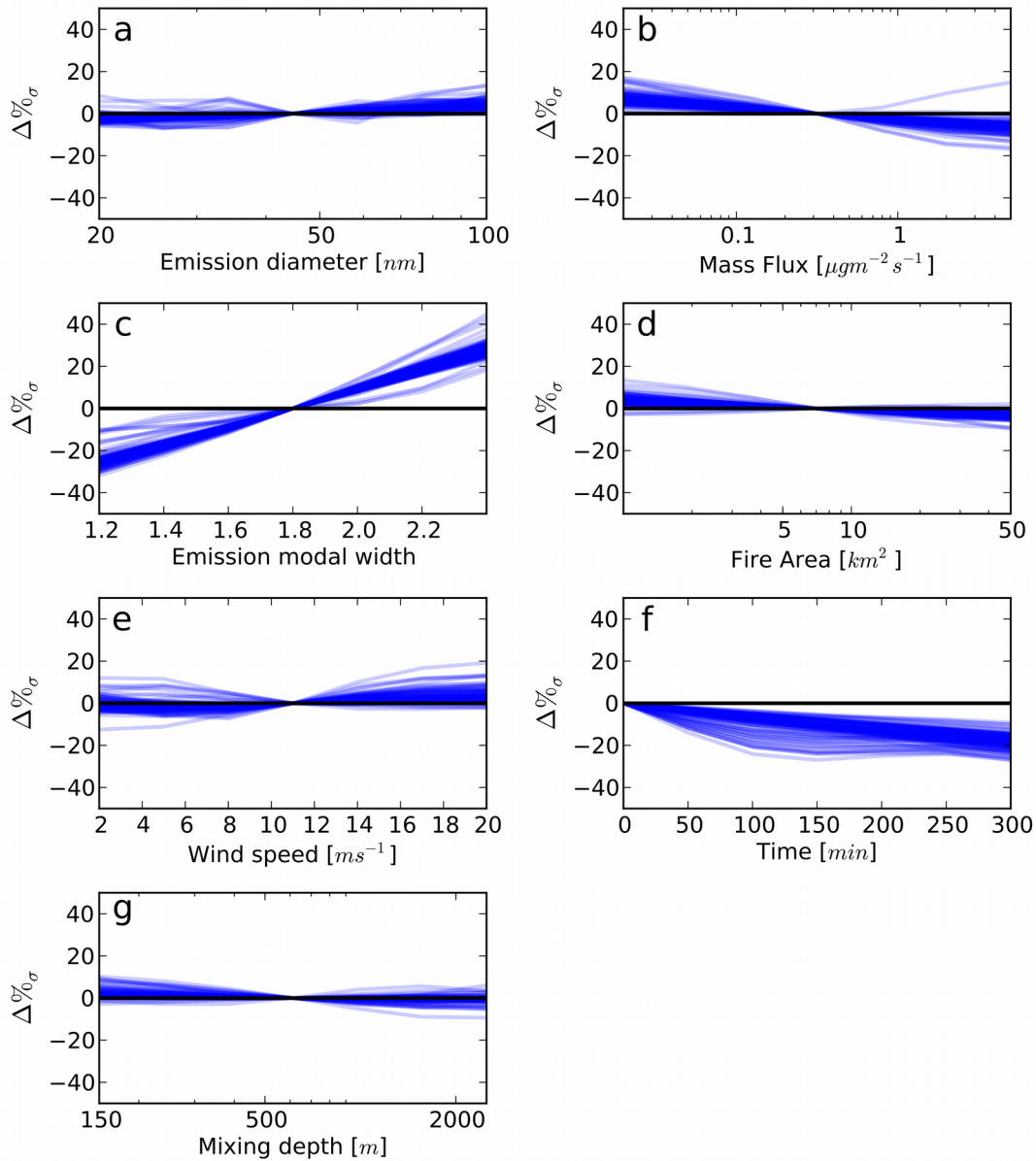


Figure 8. Sensitivity plots for the seven input parameters to the GEM-SA σ emulator parameterization. For each panel, a single input parameter is varied systematically from its minimum to maximum value for 100 randomly chosen sets of the other six parameters (100 lines in each panel). The sensitivities are shown as percent change in final σ , individually normalized to the center value of the x-axis (to zero in Time).

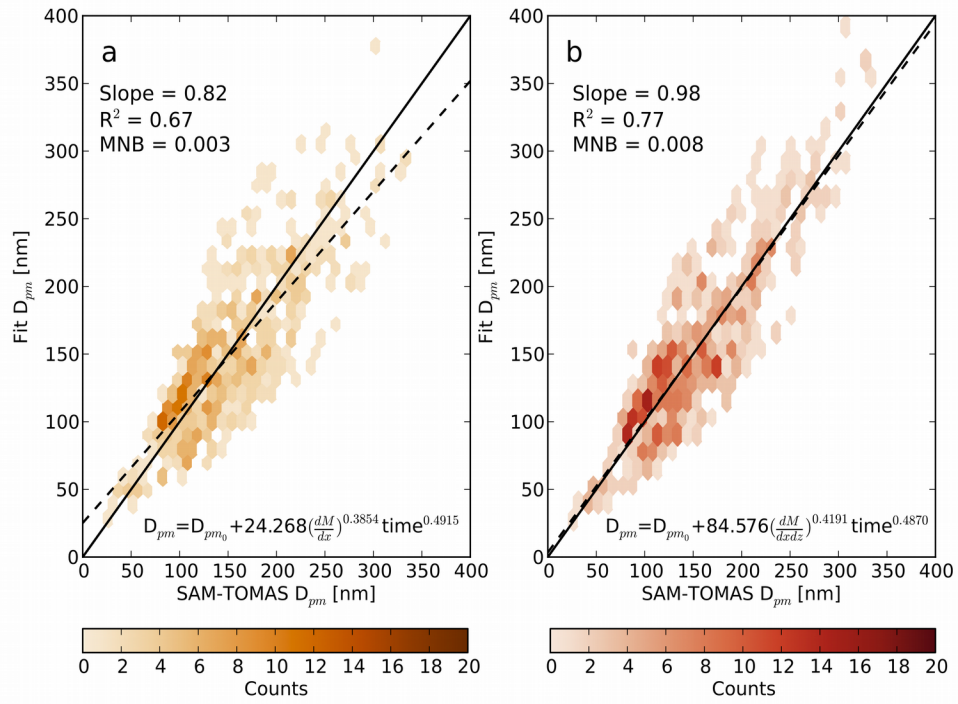


Figure 9. One-to-one plot showing simplified D_{pm} fits vs SAM-TOMAS for a) dM/dx , and b) $dM/dxdz$. The black line is the one-to-one line. The dashed black line is the line of best fit. $N = 624$.

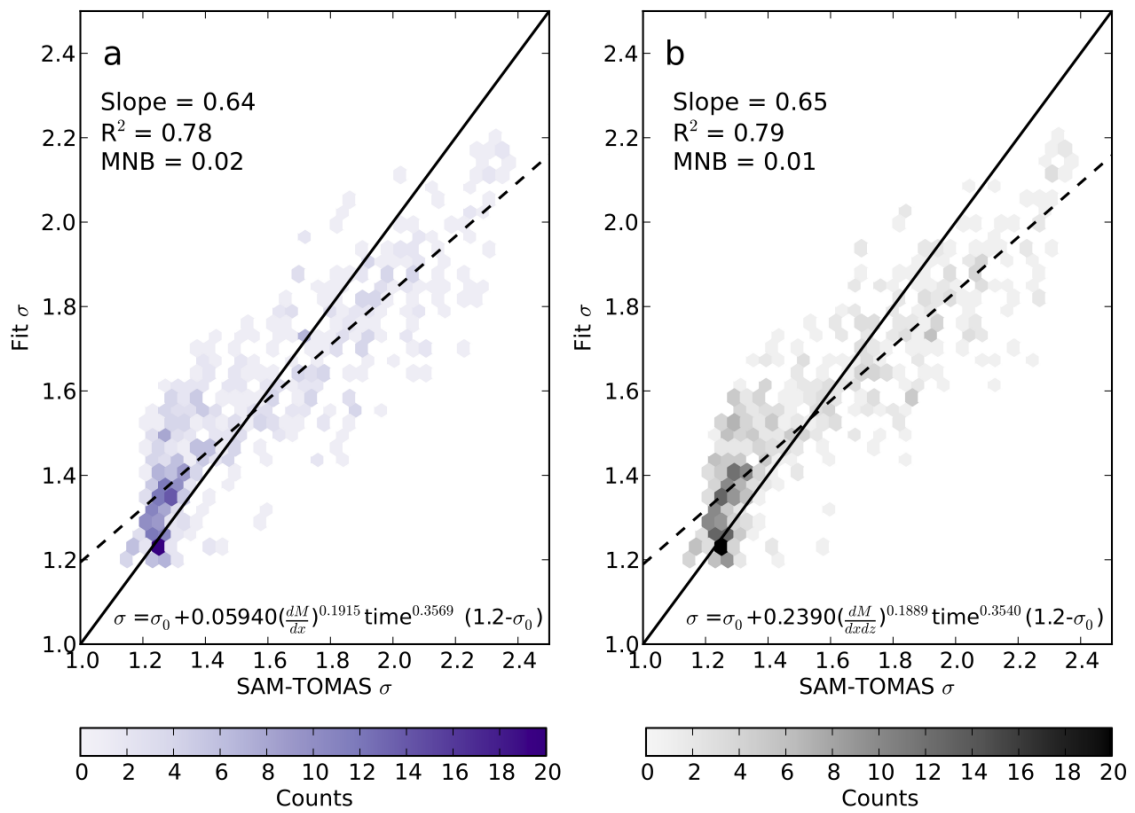


Figure 10. One-to-one plot showing simplified σ fits vs SAM-TOMAS for a) dM/dx , and b) $dM/dxdz$. The solid black line is the one-to-one line. The dashed black line is the line of best linear fit. $N = 624$.

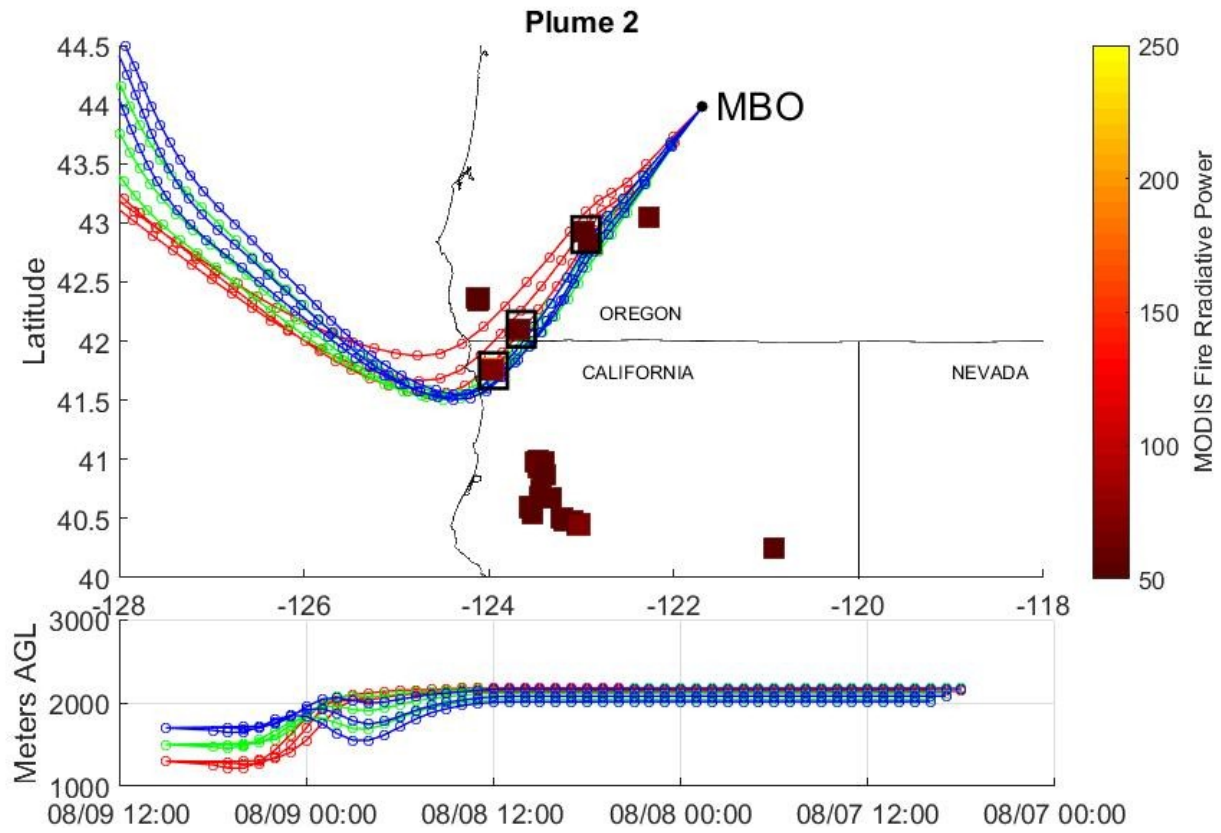


Figure 11. Back-trajectories from plume 2 observed at MBO. The colored squares represent fires during the time of the back-trajectory and are colored by Fire Radiative Power (FRP). The black squares indicate the fire areas used in the parameterization to estimate D_{pm} and σ .

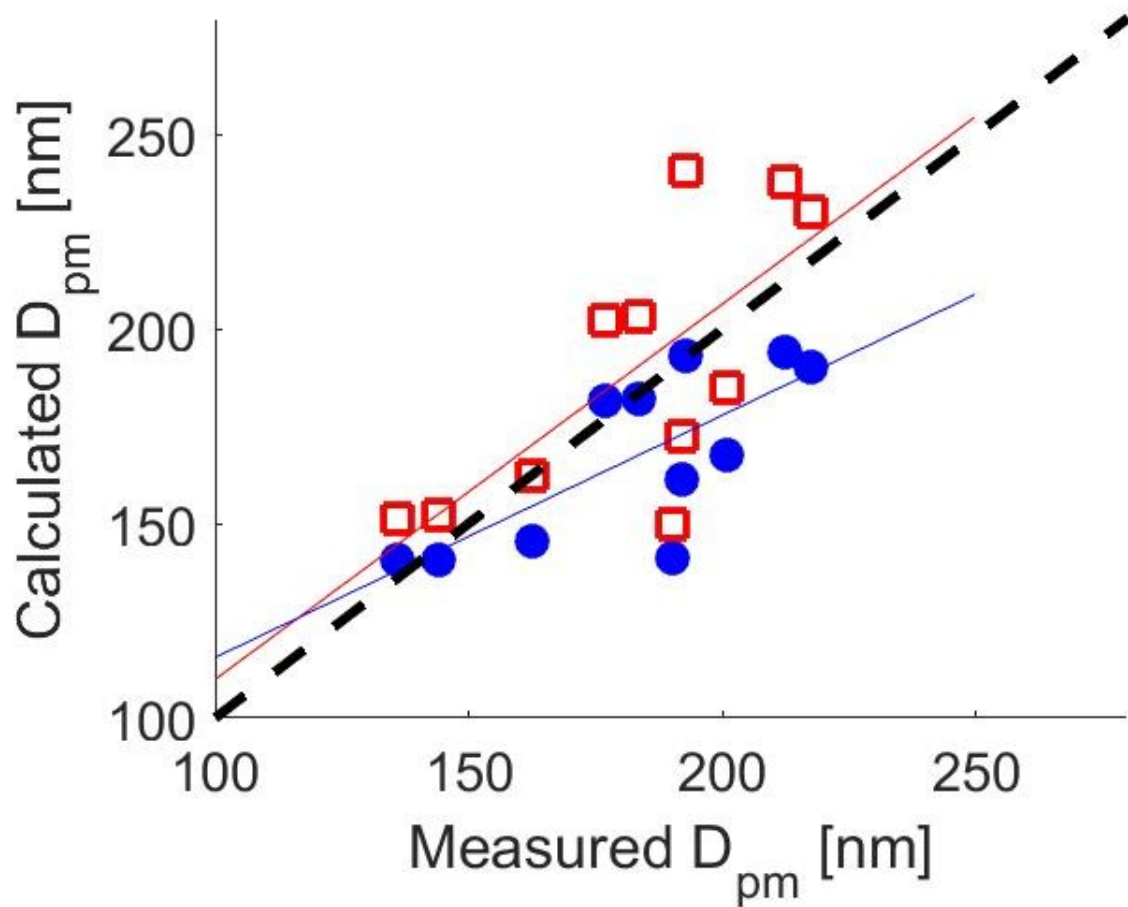


Figure 12. Scatter plot showing calculated and measured D_{pm} for biomass-burning plumes observed at MBO during August of 2015. The blue circles represent D_{pm} calculated using Eqn. 1 (dM/dx), and the red circles represent D_{pm} calculated using Eqn. 2 ($dM/dxdz$).

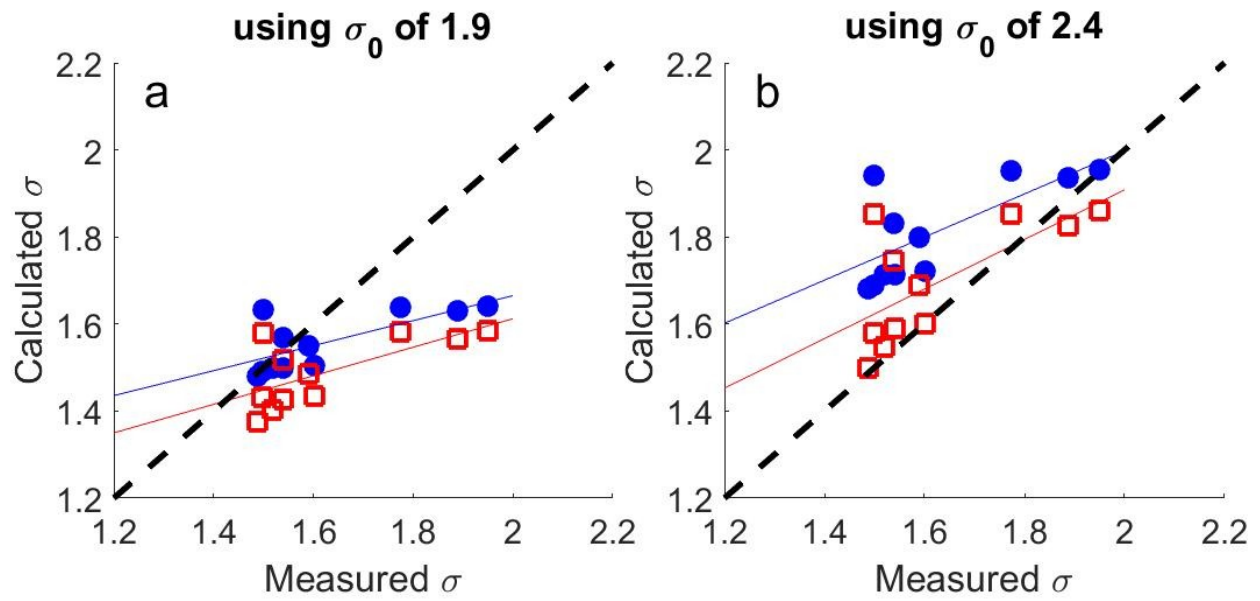


Figure 13. Scatter plots showing calculated and measured modal width (σ) for biomass-burning plumes observed at MBO during August of 2015. The blue circles represent σ calculated using Eqn. 3 (dM/dx), and the red circles represent σ calculated using Eqn 4. ($dM/dxdz$). Different emission modal width values (σ_0) were used to calculate σ , (a) used a σ_0 of 1.9 and (b) used a σ_0 of 2.4.